Astronomy & Astrophysics manuscript no. Orion-methanol-publisher
March 7, 2013

© ESO 2013

arXiv:1206.2140v1 [astro-ph.GA] 11 Jun 2012

Deuterated methanol in Orion BN/KL [⋆]

T.-C. Peng[1,2], D. Despois[1,2], N. Brouillet[1,2], B. Parise[3], and A. Baudry[1,2]

[1] Univ. Bordeaux, LAB, UMR 5804, F-33270, Floirac, France
e-mail: `Tzu-Cheng.Peng@obs.u-bordeaux1.fr`
[2] CNRS, LAB, UMR 5804, F-33270, Floirac, France
[3] Max-Planck-Institut für Radioastronomie (MPIfR), Auf dem Hügel 69, 53121 Bonn, Germany

ABSTRACT

Aims. Deuterated molecules have been detected and studied toward Orion BN/KL in the past decades, mostly with single-dish telescopes. However, high angular resolution data are critical not only for interpreting the spatial distribution of the deuteration ratio but also for understanding this complex region in terms of cloud evolution involving star-forming activities and stellar feedbacks. Therefore, it is important to investigate the deuterated ratio of methanol, one of the most abundant grain-surface species, on a scale of a few arcseconds to better understand the physical conditions related to deuteration in Orion BN/KL.

Methods. Orion BN/KL was extensively observed with the IRAM Plateau de Bure Interferometer from 1999 to 2007 in the 1 to 3 mm range. The angular resolution varies from $1''.8 \times 0''.8$ to $3''.6 \times 2''.3$ and the spectral resolution varies from 0.4 to 1.9 km s^{-1}. Deuterated methanol CH_2DOH and CH_3OD and CH_3OH lines were searched for within our 3 mm and 1.3 mm data sets.

Results. We present here the first high angular resolution ($1''.8 \times 0''.8$) images of deuterated methanol CH_2DOH in Orion BN/KL. Six CH_2DOH lines were detected around 105.8, 223.5, and 225.9 GHz. In addition, three E-type methanol lines around 101–102 GHz were detected and were used to derive the corresponding CH_3OH rotational temperatures and column densities toward different regions across Orion BN/KL. The strongest CH_2DOH and CH_3OH emissions come from the Hot Core southwest region with a velocity that is typical of the Compact Ridge ($V_{\rm LSR} \approx 8$ km s^{-1}). We derive [CH_2DOH]/[CH_3OH] abundance ratios of $0.8 - 1.3 \times 10^{-3}$ toward three CH_2DOH emission peaks. A new transition of CH_3OD was detected at 226.2 GHz for the first time in the interstellar medium. Its distribution is similar to that of CH_2DOH. Besides, we find that the [CH_2DOH]/[CH_3OD] abundance ratios are lower than unity in the central part of BN/KL. Furthermore, the HDO $3_{1,2} - 2_{2,1}$ line at 225.9 GHz was detected and its emission distribution shows a shift of a few arcseconds with respect to the deuterated methanol emission that likely results from different excitation effects. The deuteration ratios derived along Orion BN/KL are not markedly different from one clump to another. However, various processes such as slow heating due to ongoing star formation, heating by luminous infrared sources, or heating by shocks could be competing to explain some local differences observed for these ratios.

Key words. Interstellar medium (ISM), ISM: clouds, ISM: molecules, Astrochemistry

1. Introduction

Deuterium chemistry in the interstellar medium (ISM) has been intensively studied in recent decades. More and more deuterated molecules have been found as well as multiply-deuterated species, e.g., ND_3 (van der Tak et al., 2002; Lis et al., 2002) and CD_3OH (Parise et al., 2004). Deuterium chemistry models have also been revised to explain the observations that show a strong enhancement of deuterium-bearing molecule abundances in star-forming regions (e.g., Roberts et al., 2003; Roberts & Millar, 2000; Charnley et al., 1997), compared with the D/H ratio of $2 - 3 \times 10^{-5}$ in the local interstellar gas (see, e.g., Linsky et al., 2006, and references therein). Those strong enhancements (by a factor of a few thousand) are seen mostly in methanol, ammonia, water, and formaldehyde, leading to the abundance ratios > 0.1 compared with their non-deuterated analogs. The formation of these molecules can be largely explained by grain-surface reactions that provide a natural explanation for the abundant doubly or multiply deuterated molecules that ion-molecule chemistry failed to predict (Turner, 1990).

Many deuterated molecules were first detected toward the Orion Becklin-Neugebauer/Kleinmann-Low (BN/KL) region (Becklin & Neugebauer, 1967; Kleinmann & Low, 1967), one of the closest (414 ± 7 pc, Menten et al., 2007) and most-studied star-forming regions in the sky. For example, deuterated water HDO and deuterated ammonia NH_2D were first detected by Turner et al. (1975) and Rodriguez Kuiper et al. (1978), and the single-deuterated methanol molecules CH_3OD and CH_2DOH were first detected toward the same region by Mauersberger et al. (1988) and Jacq et al. (1993), respectively. Although grain-surface chemical models can well explain the high abundance of those deuterated molecules in molecular clouds, the deuteration branching ratios in the same species predicted by models disagree with observations. For instance, Charnley et al. (1997) showed that the formation of deuterated methanol on grains based on the addition of H and D atoms to CO always leads to [CH_2DOH]/[CH_3OD] abundance ratios of about 3. This prediction is in conflict with the [CH_2DOH]/[CH_3OD] ratio of 1.1–1.5 observed by Jacq et al. (1993) in Orion BN/KL. However, Rodgers & Charnley (2002) later pointed out that without taking into account other surface species such as CO and H_2CO and possibly different energy barriers involved in the reaction scheme, the [CH_2DOH]/[CH_3OD] ratio of 3 is an artificial result of the model assumptions. In addition, most proposed models that include surface chemistry strongly depend on local environment where temperature and gas density play important roles in the chemical reaction rates.

[⋆] Based on observations carried out with the IRAM Plateau de Bure Interferometer. IRAM is supported by INSU/CNRS (France), MPG (Germany), and IGN (Spain).

Table 1. Observational parameters of the PdBI data sets

Bandwidth (GHz)	Observation date	Configuration	Flux conversion (1 Jy beam^{-1})	RMS noise (mJy beam^{-1})	$\theta_{\rm HPBW}{}^{a}$ ($''$)	δv^{b} (km s^{-1})	$\theta_{\rm syn}{}^{c}$ ($'' \times ''$)	PA (°)
101.178–101.717	2003–2006	BC	15.8 K	2.9	49.7	1.85	3.79×1.99	22
105.655–105.726	2005 Aug–Nov	D	2.9 K	7.6	47.7	0.89	7.13×5.36	9
223.402–223.941	2003–2007	BC	17.3 K	21.2	22.5	0.84	1.79×0.79	14
225.805–225.942	2005 Sep–Nov	D	2.9 K	40.8	22.3	0.42	3.63×2.26	12
225.990–226.192	2005 Sep–Nov	D	2.9 K	40.8	22.3	0.42	3.63×2.25	12

Notes. $^{(a)}$ Primary beam size $^{(b)}$ Channel separation $^{(c)}$ Synthesized beam size

This is especially true for the Orion BN/KL region where contributions from stellar feedbacks (e.g., ultraviolet photons) and star formation activities (e.g., outflows/shocks) alter the warm-up history of the cloud, involving both grain surface and gas-phase chemistry. Hence, it is crucial to investigate the BN/KL deuterated methanol distribution with high spatial resolutions so that the physical conditions of individual clumps are properly constrained and the deuteration ratios can be related to specific physical processes. Additionally, deeper insight into the processes at play can be gained by comparing CH_2DOH maps with another major deuterated species, HDO.

The massive star-forming region Orion BN/KL is complicated not only because of the interactions between outflows and the ambient material, but also because of its rich and complex chemistry at the so-called Orion Hot Core and Compact Ridge regions (see, e.g., Blake et al., 1987). Owing to larger single-dish beam sizes in the early spectral line studies of Orion BN/KL, molecular line profiles were usually decomposed into several components according to their local standard of rest (LSR) velocities and line widths. The Orion hot molecular core (Hot Core) is usually characterized by its velocity component at $V_{\rm LSR}$=5–6 km s^{-1} and a broad line width of about 5–10 km s^{-1}. It has been identified in the interferometric maps as a strong mm/submm continuum emission peak close to the infrared (IR) source IRc2 (see, e.g., Gezari et al., 1998; Downes et al., 1981; Rieke et al., 1973), whereas many molecular emission peaks observed around 8 km s^{-1} are displaced from the Hot Core by about $4''$ to the southwest (Hot Core Southwest, HC-SW; see, e.g., works of Favre et al., 2011; Wang et al., 2010; Tang et al., 2010; Friedel & Snyder, 2008, and references therein).

The 8–9 km s^{-1} LSR velocity component of the Orion Compact Ridge exhibits a relatively narrow line width (3–5 km s^{-1}). The exact location of the Orion Compact Ridge is somewhat ambiguous, but recent interferometric observations (e.g., Favre et al., 2011; Friedel & Snyder, 2008) suggest that it is located $10''$–$15''$ to the southwest of the Hot Core (the strongest dust continuum peak). It is important to mention that the Orion Hot Core is located within the NE-SW dense ridge of the BN/KL region seen in dust continuum emission (Favre et al., 2011; Tang et al., 2010), and is part of the hierarchical filamentary structure seen on a larger scale in OMC-1 (e.g., mid-J CO images by Peng et al., 2012). Additionally, the Orion Compact Ridge is located at the southern part of this dense ridge, the bottom part of the V-shaped region seen in many molecular lines, e.g., CS (Chandler & Wood, 1997), SO (Wright et al., 1996), $HCOOCH_3$ (Favre et al., 2011), and NH_3 (Goddi et al., 2011).

The main goal of this paper is to investigate the deuteration ratios in Orion BN/KL, and address the possible causes for the abundant deuterated methanol in this region. We present the first high angular resolution ($1.''8 \times 0.''8$) images of CH_2DOH toward the Orion BN/KL region (§3.1). CH_3OH maps were also obtained from the same data sets with a $3.''8 \times 2.''0$ resolution (§3.2). The CH_3OD map and HDO result are shown in §3.3 and §3.4, respectively. We discuss methanol deuteration in §4.1 for CH_2DOH and §4.2 for CH_3OD. In §4.3, our own CH_3OH data are discussed in the light of the spectral line profiles obtained at much higher frequencies with *Herschel*. Comparison of our deuterated methanol and methanol maps with our deuterated water maps is presented in §4.4, and water and methanol deuteration ratios are discussed in §4.5.

2. Observations and spectroscopy

2.1. IRAM observations

The data used in this study are part of the large 1–3 mm data sets obtained from 1999 to 2007 using PdBI[1] toward the Orion BN/KL region (see Favre et al., 2011, for more observational details). Four data sets (Table 1) and five antennas equipped with two SIS receivers were used in this study. The quasars 0458–020, 0528+134, 0605–085, and 0607–157, and the BL Lac source 0420–014 were observed for phase and amplitude calibration. The six units of the correlator allowed us to achieve different bandwidths and spectral resolutions. Using the 30m single-dish data (J. Cernicharo, priv. comm.), the missing flux for the CH_2DOH lines around 223 GHz is estimated to be 20%–50%. The large uncertainty in this estimate is due to line confusion and the difficulty in determining spectral baselines in the 30m data. The missing flux in our CH_3OH line interferometric observations around 101 GHz is estimated to be $\lesssim$ 6%. As for the HDO, CH_2DOH, and CH_3OD data at 226 GHz, we compared our PdBI HDO line emission at 225896.7 MHz with the 30m data of Jacq et al. (1990), and we find that the missing flux for this HDO line is about 23% toward IRc2. Since the CH_2DOH and CH_3OD emissions are less extended than the HDO emission, the missing fluxes of CH_2DOH and CH_3OD are likely less than 23% at 226 GHz.

The PdBI data were reduced with the GILDAS[2] package, and the continuum emission was subtracted by selecting line-free channels. Our continuum emission images were presented in Favre et al. (2011) where the H_2 column densities of selected clumps were also estimated. The data cube was then cleaned channel-by-channel with the Clark algorithm (Clark, 1980) implemented in the GILDAS package.

2.2. CH_2DOH spectroscopy

CH_2DOH is an asymmetric top molecule similar to CH_3OH where one H atom is replaced by a D atom in the methyl group (–CH_3). Therefore, the threefold symmetry (C_{3V}) of the

---

[1] The IRAM Plateau de Bure Interferometer. IRAM is supported by INSU/CNRS (France), MPG (Germany) and IGN (Spain).

[2] http://www.iram.fr/IRAMFR/GILDAS/

Table 2. Spectroscopic parameters of the detected lines

Frequency[a] (MHz)	Transition (J_{k_a,k_c})	E_{up}/k (K)	$S\mu^2$ (D^2)
	CH_2DOH		
105806.4100	$11_{1,10} - 11_{0,11}\ e_1$	159.4	6.11
223422.2629	$5_{2,4} - 4_{2,3}\ e_0$	48.4	5.15
223616.1420	$5_{4,2} - 4_{4,1}, 5_{4,1} - 4_{4,0}\ e_0$	95.2	2.15[b]
223691.5380	$5_{3,3} - 4_{3,2}\ e_0$	68.2	3.96
223697.1880	$5_{3,2} - 4_{3,1}\ e_0$	68.2	3.96
225878.2540	$3_{1,3} - 2_{0,2}\ o_0$	35.7	2.28
	CH_3OH		
101185.4530	$6_{-2} - 6_1$ E	74.7	0.021
101293.4150	$7_{-2} - 7_1$ E	91.0	0.046
101469.8050	$8_{-2} - 8_1$ E	109.6	0.091
	CH_3OD		
226185.9300	$5_{-1} - 4_{-1}$ E	37.3	3.4
	HDO		
225896.7200	$3_{1,2} - 2_{2,1}$	167.6	0.69

Notes. (a) Line frequencies from this work (b) Line strength of each single line

methyl group in the internal rotation of CH_3OH is broken, and the CH_3OH symmetry states A, E1, and E2 become e_0, e_1, and o_1 in CH_2DOH, which are more difficult to deal with theoretically and experimentally (see, e.g., Lauvergnat et al., 2009; Mukhopadhyay et al., 2002), leading to only few published studies of accurate line frequency measurements to date. The CH_2DOH substate symmetry can be characterized as even (e) or odd (o) according to the plane of symmetry defined by the DCO or COH plane. For example, the minimum potential energy for CH_2DOH occurs in the "trans" substate where the D atom is opposite to OH, and the secondary minimum occurs at the "gauche" positions where the D atom is located at –120 degrees from the "trans" position (Mukhopadhyay et al., 2002). Therefore, the ground torsional states of CH_2DOH contain three substates, e_0 ("trans"), e_1 (symmetric "gauche"), and o_1 (antisymmetric "gauche") with an increasing energy, similar to ethanol (see, e.g., Pearson et al., 1997; Mukhopadhyay et al., 2002). The selection rules for the same symmetry states (e.g., $e_0 - e_0$) allow a- and b-type transitions, and c-type transitions are allowed for involving different symmetry states (e.g., $o_1 - e_1$) in CH_2DOH. The CH_2DOH molecular parameters are listed in Table 2. The CH_2DOH molecular parameters were provided by one of us (B. Parise, see Appendix A), and the CH_3OH molecular parameters were taken from the JPL database[3] (see calculations of Xu et al., 2008).

3. Results

3.1. CH_2DOH

Six CH_2DOH lines have been detected toward Orion BN/KL, and three of them are slightly blended with other molecular lines. Four CH_2DOH lines are a-type ($\Delta K_a = 0$ and $\Delta K_c = 1$) R-branch ($\Delta J = 1$) transitions with one b-type ($\Delta K_a = 1$ and $\Delta K_c = 1$) Q-branch ($\Delta J = 0$) transition and one b-type R-branch transition. The CH_2DOH line parameter measurements toward Orion BN/KL are summarized in the appendix (Table B.1).

Emission peaks: The CH_2DOH emission is mostly present in the southern part of the Orion BN/KL region, or the Compact Ridge region with a characteristic V_{LSR} of $\approx$ 8 km s^{-1}. For example, the CH_2DOH velocity channel maps in Figures 1 and B.1 show one strong peak (deuterated methanol 1, dM-1) and two weaker peaks (dM-2 and dM-3) in the 7–9 km s^{-1} velocity range.

There is no clear CH_2DOH detection at the Orion Hot Core itself (the strong dust continuum peak), except for the weak emission close to the source I position (Menten & Reid, 1995; Garay et al., 1987) shown in the CH_2DOH $5_{2,4} - 4_{2,3}$ e_0 line (see Fig. 1, V_{LSR}=5–7 km s^{-1}). Since the feature associated with source I is only seen in our strongest CH_2DOH line, it is not clear if the signal-to-noise ratio (S/N) is too low to detect this feature in other transitions, or if this feature is simply caused by contamination of other molecular lines from the region close to the Hot Core. Nevertheless, there is no indication of other molecular lines at this frequency.

The CH_2DOH spectra toward the three main peaks are shown in the appendix (Figure B.2). The average V_{LSR} measured at the peak emission channel is 7.7 ± 0.4 km s^{-1} for dM-1, 7.8 ± 0.4 km s^{-1} for dM-2, and 7.8 ± 0.4 km s^{-1} for dM-3. The FWHM line widths estimated by fitting a Gaussian profile are 2.1 ± 1.2 km s^{-1} and 2.3 ± 0.9 km s^{-1} for dM-1 and dM-2, respectively. The weak dM-3 source exhibits a line width of approximately 3.7 ± 0.5 km s^{-1}, which is broader than the dM-1 and dM-2 line widths; this is likely because of the blending of two or more velocity components (see below).

Additionally, dM-1 has a counterpart in the methyl formate emission (MF-2) observed by Favre et al. (2011), and dM-2 and dM-3 are nearly coinciding with MF-3 and MF-1, respectively. It should be noted that MF-1, the strongest methyl formate emission peak in Orion BN/KL (Favre et al., 2011), shows weak CH_2DOH emission in our data (dM-3). As shown by Favre et al. (2011), MF-1 exhibits two velocity components at 7.5 km s^{-1} and 9.2 km s^{-1}, and these two components are only seen in the 225878.3 MHz CH_2DOH line toward dM-3 where our spectral resolution is higher (0.42 km s^{-1}). Furthermore, dM-2 and dM-3 are close to the CH_3OH emission peak in the SMA CH_3OH and $^{13}CH_3OH$ images ($\theta_{syn} \approx 1\farcs1 \times 0\farcs9$, E_{up}/k = 110 – 730 K) obtained by Beuther et al. (2005) around 337 GHz. It is interesting to note that dM-2 is close to the 25 GHz and 95 GHz CH_3OH maser emission peaks reported by Matsakis et al. (1980) and Plambeck & Wright (1988), respectively.

Population diagrams: We use population diagrams to estimate the column density of CH_2DOH (e.g., Goldsmith & Langer, 1999; Turner, 1991)

$$\ln\frac{N_{up}}{g_{up}} = \ln\frac{3k\int T_B dV}{8\pi^3\nu S\mu^2} = \ln\frac{N}{Q} - \frac{E_{up}}{kT_{rot}}, \quad (1)$$

where N is the total column density, T_{rot} the rotational temperature, S the line strength, and μ the dipole moment (μ_x = 1.44 D and μ_z = 0.89 D, Ivash & Dennison, 1953). In this work, the partition function Q is calculated according to our approximation $Q = 2.25\ T^{1.5}$. We used the four CH_2DOH lines at 223 GHz (e_0 state) observed with the same spatial resolution in this population diagram analysis. Because our data points fall in a narrow energy range, the population diagrams give a temperature of about 100 K with a very large uncertainty. Hence, the rotational temperatures were assumed and taken from the work of Favre et al. (2011) to reduce the statistical error. We assumed here that both CH_3OH and $HCOOCH_3$ trace the same gas because both lines show the same emission peaks, V_{LSR}, and ΔV.

---

[3] http://spec.jpl.nasa.gov/

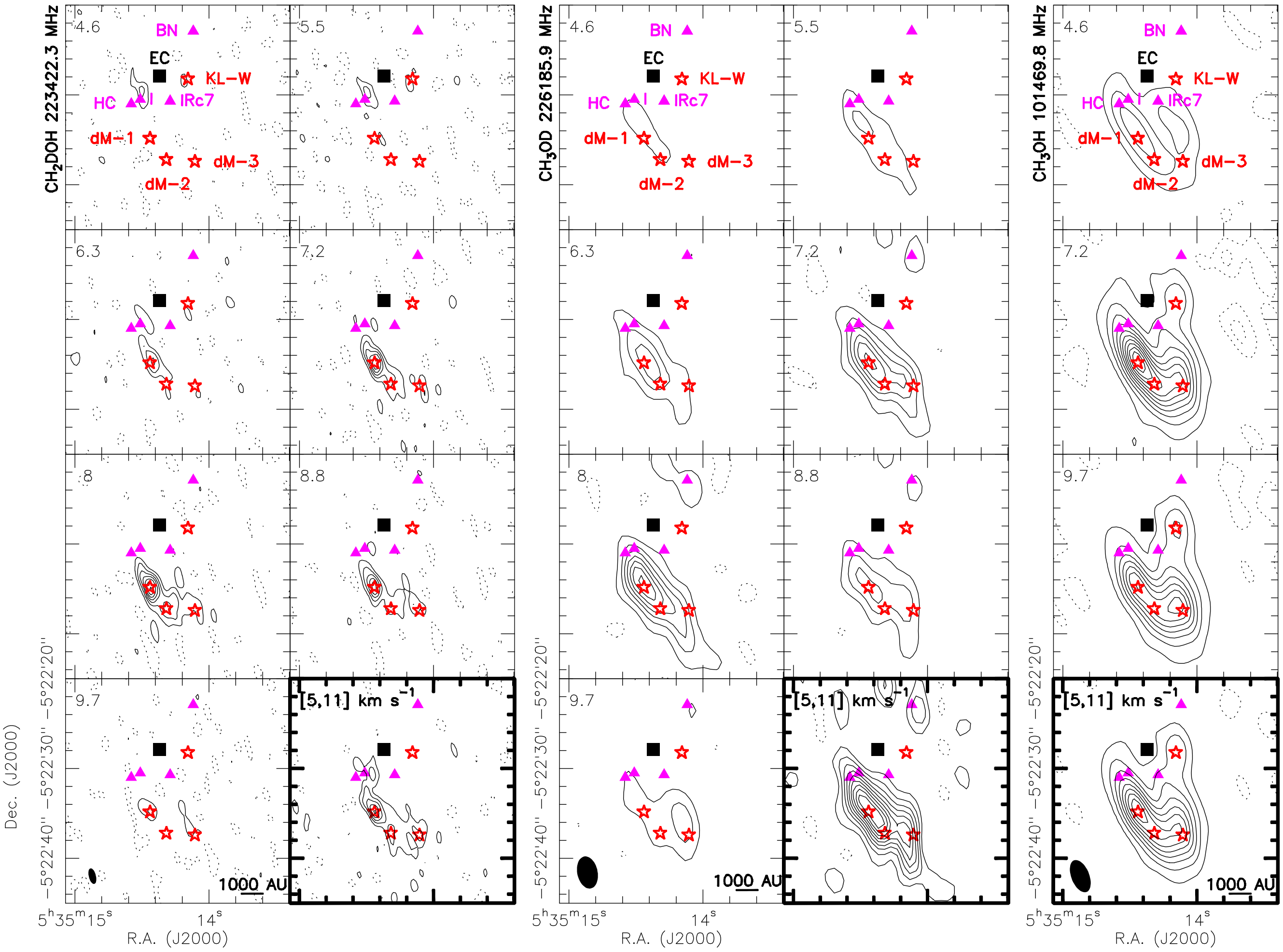

Fig. 1. Left: Channel maps of the CH$_2$DOH $5_{2,4} - 4_{2,3}$ ($E_{up}/k = 95.2$ K) emission at 223422.3 MHz for a synthesized beam of $1''.8 \times 0''.8$. Contours run from 40 mJy beam^{-1} (2 σ) to 280 mJy beam^{-1} (4.84 K) in steps of 40 mJy beam^{-1}, and the dashed contours represent –20 mJy beam^{-1}. The bottom-right panel shows the integrated intensity (from 5 to 11 km s^{-1}) in contours running from 0.2 to 1.0 Jy beam^{-1} km s^{-1} in steps of 0.2 Jy beam^{-1} km s^{-1}, and the dashed contours represent –0.08 Jy beam^{-1} km s^{-1}. Middle: Channel maps of the CH$_3$OD emission at 226185.9 MHz ($E_{up}/k = 37.3$ K) for a synthesized beam of $3''.6 \times 2''.3$. Contours run from 0.12 to 2.52 Jy beam^{-1} in steps of 0.04 Jy beam^{-1} (3 σ), and the dashed contours represent –0.08 Jy beam^{-1}. The bottom-right panel shows the integrated intensity of CH$_3$OD (from 5 to 11 km s^{-1}) in contours running from 10% to 90% in step of 10% of the peak intensity (3.1 Jy beam^{-1} km s^{-1}), and the dashed contours represent –10% of the peak intensity. Right: Channel maps of the CH$_3$OH $8_{-2} - 8_1$ E ($E_{up}/k = 109.6$ K) emission at 101469.8 MHz for a synthesized beam of $3''.8 \times 2''.0$. Contours run from 40 to 490 mJy beam^{-1} (7.74 K) in steps of 50 mJy beam^{-1}. The dashed contours represent –30 (1 σ) and –90 mJy beam^{-1}. The bottom panel shows the integrated intensity of CH$_3$OH (from 5 to 11 km s^{-1}) in contours running from 0.3 to 3.0 Jy beam^{-1} km s^{-1} in steps of 0.3 Jy beam^{-1} km s^{-1}, and the dashed contours represent –0.03 Jy beam^{-1} km s^{-1}. The black square marks the center of explosion according to Zapata et al. (2009). The positions of source BN, source *I*, the Hot Core (HC), and IRc7 are marked by magenta triangles. The positions of deuterated methanol emission peaks (dM-1, dM-2, and dM-3) and KL-W are marked by red stars. Note that the channel separation in the CH$_3$OD channel maps are resampled and only the three selected CH$_3$OH channel maps are shown here for clarity (see Fig. B.1 for the full CH$_3$OH channel maps).

Figure B.3 shows the least-squares fit result where we assumed that the rotational temperatures according to the HCOOCH$_3$ excitation temperatures are 130 K for dM-1 and 85 K for dM-2 as derived by Favre et al. (2011) with the same spatial resolution ($1''.79 \times 0''.79$). The derived CH$_2$DOH column densities are given in Table 3. We find $8.8 \pm 0.9 \times 10^{15}$ cm^{-2} and $2.4 \pm 0.3 \times 10^{15}$ cm^{-2} for dM-1 and dM-2, respectively. Adopting an H$_2$ column density of 3.1×10^{24} cm^{-2} as derived by Favre et al. (2011) from the 223 GHz dust continuum, we obtain a CH$_2$DOH relative abundance of $2.8 \pm 0.3 \times 10^{-9}$ toward dM-1. The relative CH$_2$DOH abundance is uncertain toward dM-2 because this clump does not have a strong dust continuum emission and no reliable H$_2$ column density can be derived.

Jacq et al. (1993) derived a CH$_2$DOH column density of $2.6 - 5.4 \times 10^{15}$ cm^{-2} toward Orion IRc2 with an estimated temperature of 88 K and an assumed source size of 15″ from their IRAM 30m data. When smoothing our CH$_2$DOH data to a source size of 15″, the derived CH$_2$DOH column density is $0.2 - 1.4 \times 10^{15}$ cm^{-2}, assuming a maximum missing flux of 50% and an excitation temperature of 88 K toward IRc2. The column density disagrees with that of Jacq et al. (1993) by a factor of 2–3. Owing to the importance of deuteration ratios, which are obtained based mainly on previous single-dish estimates, we

Table 3. Derived column density and temperature for CH_2DOH and CH_3OH

Position	R.A.	Dec.	Size	$T_{\mathrm{rot}}(CH_2DOH)$	$N(CH_2DOH)$	$T_{\mathrm{rot}}(CH_3OH)$	$N(CH_3OH)$	$[CH_2DOH]/[CH_3OH]$
	$05^{\mathrm{h}}35^{\mathrm{m}}$	$-05^\circ22'$		(K)	(cm^{-2})	(K)	(cm^{-2})	
dM-1	...$14^{\mathrm{s}}.442$	...$34''.86$	$1''.8 \times 0''.8$	130^a	$8.8 \pm 0.9 \times 10^{15}$	...	...	...
			$3''.8 \times 2''.0$	130^a	$4.7 \pm 0.5 \times 10^{15}$	130^a	$4.2 \pm 0.4 \times 10^{18}$	$1.1 \pm 0.2 \times 10^{-3}$
			$3''.8 \times 2''.0$	60	$2.4 \pm 0.3 \times 10^{15}$	60.3 ± 3.7	$2.1 \pm 0.3 \times 10^{18}$	$1.1 \pm 0.2 \times 10^{-3}$
dM-2	...$14^{\mathrm{s}}.320$	...$37''.23$	$1''.8 \times 0''.8$	85^a	$2.4 \pm 0.3 \times 10^{15}$	...	...	...
			$3''.8 \times 2''.0$	85^a	$1.7 \pm 0.1 \times 10^{15}$	85^a	$2.2 \pm 0.7 \times 10^{18}$	$7.7 \pm 2.5 \times 10^{-4}$
			$3''.8 \times 2''.0$	66	$1.4 \pm 0.2 \times 10^{15}$	66.2 ± 4.7	$1.9 \pm 0.3 \times 10^{18}$	$7.4 \pm 1.6 \times 10^{-4}$
dM-3	...$14^{\mathrm{s}}.107$	...$37''.43$	$1''.8 \times 0''.8$	58	$9.5 \pm 4.5 \times 10^{14}$	...	...	...
			$3''.8 \times 2''.0$	58	$1.5 \pm 0.1 \times 10^{15}$	57.6 ± 1.8	$1.7 \pm 0.1 \times 10^{18}$	$8.8 \pm 0.8 \times 10^{-4}$
KL-W	...$14^{\mathrm{s}}.159$	...$28''.25$	$1''.8 \times 0''.8$	44	$< 3.0 \times 10^{14}$	...	...	...
			$3''.8 \times 2''.0$	44	$< 2.0 \times 10^{14}$	43.7 ± 4.3	$9.2 \pm 2.1 \times 10^{17}$	$< 2.2 \times 10^{-4}$

Notes. The $[CH_2DOH]/[CH_3OH]$ ratios are derived only for the $3''.8 \times 2''.0$ clump size. For dM-1 and dM-2, the CH_2DOH column densities are derived from the population diagrams, and CH_3OH column densities and temperatures are derived for all sources from the population diagrams. The CH_2DOH column density of dM-3 is derived only from the $5_{2,4} - 4_{2,3}\ e_0$ line at 223422.3 MHz, assuming a rotational temperature of 58 K (estimated from CH_3OH). The positions of dM-1, dM-2, dM-3, and KL-W are given at Epoch J2000.0. $^{(a)}$ The methyl formate rotational temperatures derived by Favre et al. (2011) are adopted here for CH_2DOH and CH_3OH.

have revised the CH_2DOH column density calculations together with CH_3OD in Appendix A to compare them with our interferometric results. We find that the CH_2DOH column density obtained by Jacq et al. (1993) is overestimated by a factor of 2–3, and the revisited value is thus consistent with our result mentioned above.

3.2. CH_3OH

Three E-type methanol lines around 101 GHz (see Table 2) have been detected; the line parameters toward different peaks are summarized in Table B.2. The CH_3OH emission exhibits a V-shaped structure (Figs. 1 and B.1) similar to that observed for several other molecular lines and for dust continuum emission. The eastern side of the V-shaped structure follows the dense ridge, and the bottom part coincides with the Compact Ridge region. The western part of this V-shaped structure lies in the N-S direction, and one CH_3OH emission peak (Orion KL western clump, KL-W, Wright et al., 1992; MF-4/5, Favre et al., 2011) is located to the north close to the IR source IRc6, which lies $\sim 3''$ north of IRc7 (see, e.g., Gezari, 1992; Gezari et al., 1998). Because of the lower spatial resolution ($3''.79 \times 1''.99$) of these CH_3OH lines, only dM-1, dM-3, and KL-W are spatially resolved. The average FWHM line width toward the CH_3OH emission peaks is 4.4 ± 1.2 km s^{-1}, and the average line width at KL-W is about 6.5 km s^{-1}, which is likely due to the blending of two or more velocity components at 8 and 10–11 km s^{-1} close to MF-4 and MF-5 (Favre et al., 2011). In addition, the E-type methanol lines' average velocity is 8.2 ± 0.9 and 8.6 ± 0.9 km s^{-1} toward the three CH_2DOH emission peaks and KL-W, respectively. Since KL-W is located $\sim 7''$ from the Hot Core and $\sim 10''$ from the Compact Ridge, the 8 km s^{-1} velocity component observed in single-dish observations ($\theta_{\mathrm{MB}} > 20''$) may contain a large amount of gas ($\sim$ 25% of our CH_3OH total flux) from the KL-W region or the western side of the V-shaped structure. This will affect the analysis based only on the velocity components.

Because the CH_3OH lines are optically thick in most cases (e.g., Menten et al., 1988), we first estimated the optical depth of the CH_3OH lines detected here around 101 GHz. In the Rayleigh-Jeans approximation we derive the opacity from

$$\tau = -\ln\left[1 - \frac{T_{\mathrm{b}} - T_{\mathrm{bg}}}{T_{\mathrm{ex}} - T_{\mathrm{bg}}}\right], \qquad (2)$$

where T_{b} and T_{ex} are the source brightness and excitation temperatures (using the derived rotational temperatures of 40–70 K), T_{bg} is the background emission temperature, including both the cosmic microwave background radiation (2.73 K) and the Orion dust emission (around 0.8–1.4 K from the PdBI data, correcting for a high interferometric filtering loss in continuum of 90%). The average CH_3OH optical depth is estimated to be $\lesssim 0.2$ for the three 101 GHz CH_3OH lines. Therefore, in the optically thin case, we can apply the population diagram method to estimate the E-type methanol column densities and rotational temperatures. The population diagrams are shown in Figure B.4 and the derived excitation temperatures and column densities are listed in Table 3.

Rotational temperatures of 40–70 K and column densities of about 10^{18} cm^{-2} are found toward selected clumps in Orion BN/KL, assuming an A/E methanol abundance ratio of 1.2 (Menten et al., 1988). The derived CH_3OH column densities are higher than the IRAM 30m result of Menten et al. (1988), who obtained a CH_3OH column density of $3.4 \pm 0.3 \times 10^{17}$ cm^{-2} with a rotational temperature of 128 ± 10 K, including both narrow and broad components and assuming a source size of $25''$. To compare ours with their results, we smoothed our CH_3OH spectra to the beam size ($25''$) of the 30m telescope at 101–102 GHz (Fig. B.5). We derived a CH_3OH column density of $2.3 \pm 0.5 \times 10^{17}$ cm^{-2} with a rotation temperature of about 60 K at the same position as used by Menten et al. (1988). Additionally, by adopting a higher temperature of 130 K, we derived a CH_3OH column density of $4.6 \pm 0.4 \times 10^{17}$ cm^{-2}, which is close to the column density derived by Menten et al. (1988).

Our methanol rotational temperature estimate is lower than the 100–150 K obtained by Menten et al. (1988) using the 30m telescope and lower than the 80 K of Neill et al. (2011) using CARMA, but lies at the low end of the 50–350 K obtained by Beuther et al. (2005) using SMA. Lower rotational temperatures may be due to the non-LTE behavior (or subthermal excitation, see § 4.3) of methanol. In addition, choosing only the lower-E_{up} transitions tends to result in a lower excitation temperature from population diagrams (see, e.g., Blake et al., 1987; Parise et al., 2002). Nevertheless, column densities are not very sensitive to rotational temperatures in this temperature range (Fig. B.6), and the differences in CH_3OH column densities derived with different temperatures are less than a factor of about 3.

3.3. CH_3OD

A new transition of CH_3OD ($5_{-1} - 4_{-1}$ E) was detected at 226185.9 MHz for the first time in the ISM at the edge of our spectrometer and imaged toward Orion BN/KL. The CH_3OD spectra for the selected sources in Orion BN/KL are shown in Figure 2, and the line parameters are listed in Table B.3. The CH_3OD channel maps are shown in Figure 1. The CH_3OD and CH_2DOH spatial distributions are very similar (see Fig. 3 c), and both maps show the strongest emission at dM-1 with weaker emission toward dM-2 and dM-3. The line widths of CH_3OD toward dM-1 and dM-2 are about 2–3 km s^{-1}, whereas two velocity components are clearly seen toward dM-3 with line widths of about 1–2 km s^{-1}.

3.4. HDO

In one of our low angular resolution data sets ($3''\!.6 \times 2''\!.3$), we detected one HDO line at 225896.7 MHz ($3_{1,2} - 2_{2,1}$). This is not sufficient for a detailed analysis, but it allows us to compare the spatial distribution and spectra between deuterated methanol and water emissions. Figure 2 clearly shows that the optically thin lines from rarer isotopologs of methanol have similar spectral profiles with an average line width of about 3 km s^{-1} and LSR velocities of about 8 km s^{-1} at dM-1, dM-2, and dM-3. On the other hand, the HDO spectra in Orion BN/KL have broader line widths, which are likely composed by two or more velocity components. For example, the HDO spectra at dM-1 can be decomposed by two components at LSR velocities of about 5 and 7 km s^{-1} with line widths of about 10 and 4 km s^{-1}, respectively. The narrow line feature is likely produced by the same gas at which isotopologic methanol lines have been detected, and the broad line feature may be due mainly to the shock-heated gas associated with the Hot Core and source *I* region where the hot ammonia and highly excited CH_3CN are present (see, e.g., Goddi et al., 2011; Zapata et al., 2011).

4. Discussion

4.1. The CH_2DOH/CH_3OH abundance ratios

To investigate the CH_3OH deuteration across the Orion BN/KL region, we smoothed our CH_2DOH data to the spatial resolution of the E methanol lines ($3''\!.8 \times 2''\!.0$) and derived the population diagram (Fig. B.3) by using methanol rotational temperatures and $HCOOCH_3$ rotational temperatures for low and high temperature reference, respectively (see Table 3, which summarizes our calculations toward different clumps in Orion BN-KL). The $[CH_2DOH]/[CH_3OH]$ abundance ratios are $1.1 \pm 0.2 \times 10^{-3}$, and $7.4 \pm 1.6 \times 10^{-4}$, and $8.8 \pm 0.8 \times 10^{-4}$ for dM-1, dM-2, and dM-3 with lower temperatures, respectively. An upper limit of about 2×10^{-4} is given for the $[CH_2DOH]/[CH_3OH]$ abundance ratio at KL-W. It is interesting to note that the $[CH_2DOH]/[CH_3OH]$ ratio of dM-3 is higher than that of dM-2.

These abundance ratios do not depend much on the assumed $T_{\rm rot}$ (see Fig. B.6). If higher excitation temperatures are adopted (e.g., 130 K for dM-1 and 85 K for dM-2), the $[CH_2DOH]/[CH_3OH]$ ratios do not change much. These ratios (observed toward different clumps in Orion BN/KL, see Table 3) are about one order of magnitude lower than the ratio (0.01–0.08) reported by Jacq et al. (1993). However, the $[CH_2DOH]/[CH_3OH]$ abundance ratios derived for the selected sources ($0.8 - 1.3 \times 10^3$) are consistent with a revised ratio of $0.8 - 2.8 \times 10^3$, where possible line blending and different observing positions were taken into account in the revisited calculations of the 30m observations (see Appendix A for more details). In addition, the $[CH_2DOH]/[CH_3OH]$ ratios in Orion BN/KL are lower than the deuterated methanol and formaldehyde abundance ratios estimated in several low-mass protostars, e.g., up to about 0.6 for $[CH_2DOH]/[CH_3OH]$ and 0.3 for $[HDCO]/[H_2CO]$ in Class 0 sources (Parise et al., 2006).

Assuming that both CH_2DOH and CH_3OH are in LTE and have the same excitation temperature, we can produce a $[CH_2DOH]/[CH_3OH]$ ratio map by using two transitions of CH_2DOH and CH_3OH and taking into account their line strengths, partition functions, and upper-state energies, the same method as used recently by Ratajczak et al. (2011). In the $[CH_2DOH]/[CH_3OH]$ ratio map (Fig. 3 d), dM-1 exhibits a higher ratio than observed toward the southern part of Orion BN/KL where dM-2 and dM-3 are located. It is interesting to note that the source *I* region also shows higher CH_2DOH/CH_3OH intensity ratios on each side of the bipolar outflow (marked with a double black arrow in the image). Since the feature associated with source *I* is only seen in the strongest CH_2DOH line at 223422.3 MHz, more observations are needed to confirm this result. Because we derive an upper limit of 2.2×10^{-4} for the $[CH_2DOH]/[CH_3OH]$ abundance ratio toward KL-W, which is well below the ratios derived for dM-1, dM-2, and dM-3, there might be different physical and/or chemical conditions at KL-W. Nevertheless, we cannot exclude yet that the non-detection of the CH_2DOH emission toward KL-W may result from spatial filtering in our PdBI interferometric data.

The deuteration ratios derived here are not markedly different from one clump to another except perhaps for KL-W (where an upper limit is derived). However, it is clear that the deuteration ratio tends to decrease from the dense clumps (dM-1 to dM-3) to the more extended gas in Orion BN/KL. The H_2 column densities of dM-1 and dM-3 are about $3 - 5 \times 10^{24}$ cm^{-2}, but the rotational temperature of $HCOOCH_3$ toward dM-1 (about 130 K) is higher than toward dM-2 and dM-3 (about 80 K). Therefore, the slight difference observed in the deuteration ratios is likely due to different gas temperatures of the clumps. Based on our present knowledge, we suggest that various competing processes could be at work. For instance, global, slow heating of the Orion BN/KL region through ongoing star formation should produce widespread effects and the expected net result is a fairly homogeneous deuterated ratio. On the other hand, heating by luminous infrared sources (e.g., in the vicinity of source *I*) could result in a higher temperature in this region, leading to a higher deuteration ratio toward dM-1.

4.2. The CH_2DOH/CH_3OD abundance ratios

Although only one CH_3OD line ($5_{-1} - 4_{-1}$ E at 226185.9 MHz, $E_{\rm up}/k$ = 37.3 K) has been detected in our observations, a similar $[CH_2DOH]/[CH_3OD]$ abundance ratio image can be produced in the same fashion as $[CH_2DOH]/[CH_3OH]$ by using the CH_2DOH $3_{1,3} - 2_{0,2}$ o_0 line ($E_{\rm up}/k$ = 35.7 K) at 225878.3 MHz. Figure 3 (e) shows the $[CH_2DOH]/[CH_3OD]$ abundance ratio image by assuming the same excitation temperature for CH_2DOH and CH_3OD, the method used for the $[CH_2DOH]/[CH_3OH]$ ratio map. This abundance ratio does not depend much on the temperature (see Fig. B.6 b). Our results show that the $[CH_2DOH]/[CH_3OD]$ abundance ratios are less than unity in the central region of Orion BN/KL and the mean ratio is 0.7 ± 0.3, which also differs from the ratio (1.1–1.5) reported by Jacq et al. (1993). However, the revisited calculation as mentioned above (Appendix A) of the previ-

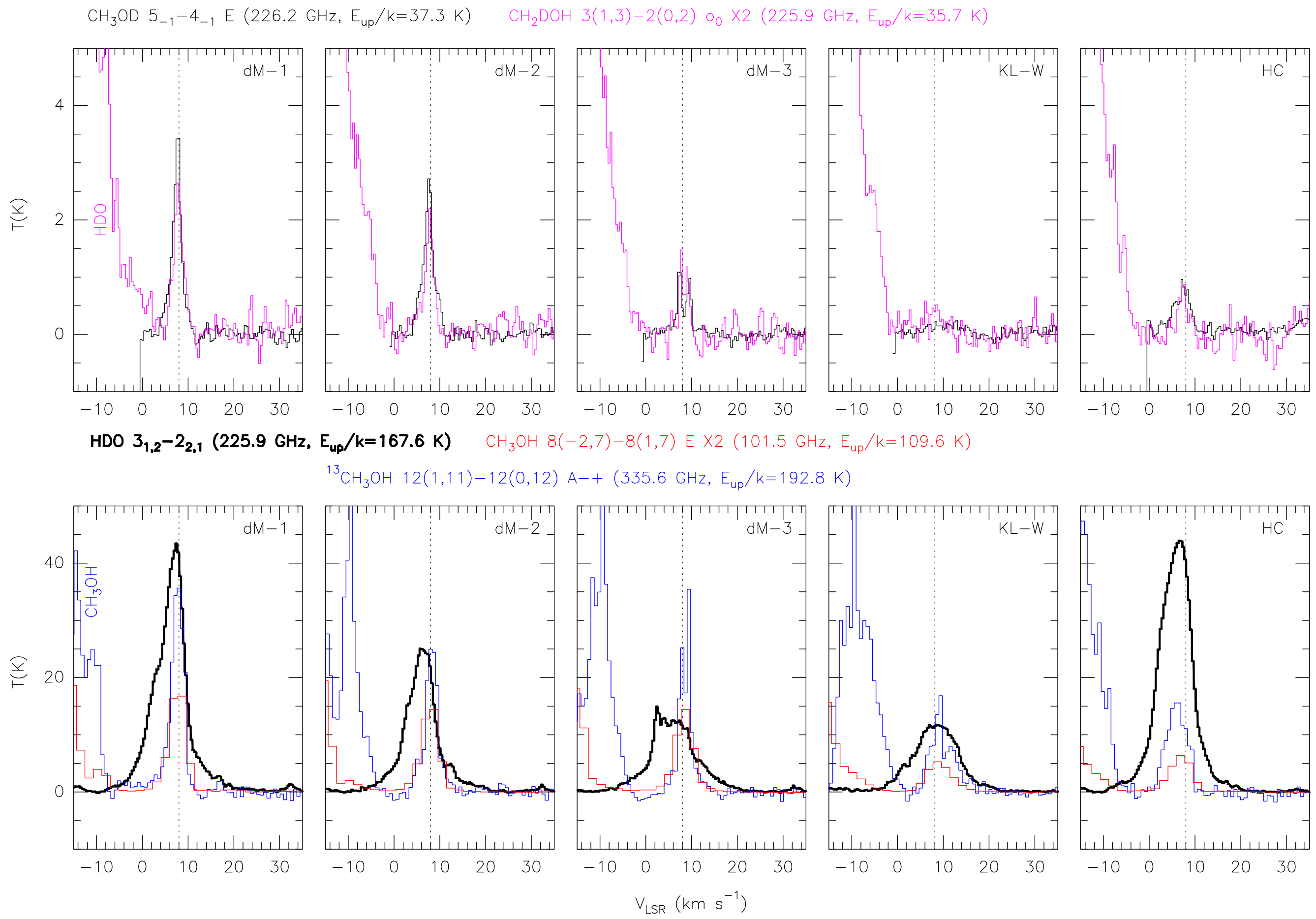

Fig. 2. Spectrum comparison of HDO, CH_3OH, $^{13}CH_3OH$, CH_2DOH, and CH_3OD toward selected sources in Orion BN/KL with a similar resolution of about 3″. The SMA $^{13}CH_3OH$ line (Y.-W. Tang, priv. comm.) is plotted in blue for a synthesized beam of 3.″0 × 2.″0. The CH_3OH line is plotted in red for a synthesized beam of 3.″8 × 2.″0. The HDO (thick black lines), CH_3OD (thin black lines), and CH_2DOH (magenta) lines are plotted for a synthesized beam of 3.″6 × 2.″3. Dotted lines indicate a $V_{\rm LSR}$ of 8 km s^{-1}. Note that the spectrum intensities of CH_3OH and CH_2DOH are multiplied by 2. Clearly, the spectra of methanol isotopologs have narrow line widths compared with those of HDO.

ous 30m observations of CH_2DOH (Jacq et al., 1993), CH_3OD (Mauersberger et al., 1988), and CH_3OH (Menten et al., 1988) gives a lower [CH_2DOH]/[CH_3OD] abundance ratio of $\lesssim 0.6$ toward IRc2 (adopting a source size of 15″), which is consistent with our results and is much lower than the values derived in low-mass protostars (e.g., Parise et al., 2002; Ratajczak et al., 2011). Additionally, we note that the [CH_2DOH]/[CH_3OD] abundance ratios are higher at dM-1 and dM-3 compared with that at dM-2.

The fact that the [CH_2DOH]/[CH_3OD] ratios are less than unity in the central Orion BN/KL region is surprising because most of the theoretical and experimental studies on deuterated methanol predict more abundant CH_2DOH than CH_3OD (see, e.g., Charnley et al., 1997; Osamura et al., 2004; Nagaoka et al., 2005; Ratajczak et al., 2009). Since CH_2DOH and CH_3OD have very similar emission distributions in Orion BN/KL, their formations seem to be closely related. As shown by Osamura et al. (2004), exchanging protons and deuterons on the two different parts of the methanol backbone is very inefficient in the post-evaporative gas-phase. However, the simulations of Osamura et al. (2004) show that the water vapor that evaporates from the surface above 80 K strongly affects the abundance of CH_3OD, because the protonation of H_2O and HDO in gas phase leads to additional fractionation throughout the reaction network. Therefore, the observed abundance ratio between CH_2DOH and CH_3OD might not reflect the primitive abundance ratio in the ice mantle of grain surfaces. This may explain the much lower [CH_2DOH]/[CH_3OD] ratios seen in Orion BN/KL, where most of the regions have higher temperatures than 80 K. Besides, it indicates that H_2O and HDO may be two critical molecules for understanding the formation processes of deuterated methanol in Orion BN/KL.

4.3. CH_3OH subthermal excitation?

Recently, Wang et al. (2011) detected more than 300 methanol lines around 524 GHz ($\theta_{\rm MB} \approx 43''$) and 1061 GHz ($\theta_{\rm MB} \approx 20''$) with the *Herschel*/HIFI instrument. Although these data were obtained with a broad beamwidth, it may be useful to investigate the implications of the Wang et al. results on our own data in terms of CH_3OH excitation. The narrow and broad CH_3OH components observed by Wang et al. show average FWHM line widths of 2.7 and 4–11 km s^{-1} at $V_{\rm LSR}$ = 8.6 and 6–9 km s^{-1}, respectively. Their LSR velocities are consistent with our data. However, their broad components' line widths are wider than ours. This is likely due to optical depth broadening ($\tau \sim 15$ in the *Herschel*/HIFI CH_3OH data), although we cannot exclude that some faint broad and extended velocity components detected by

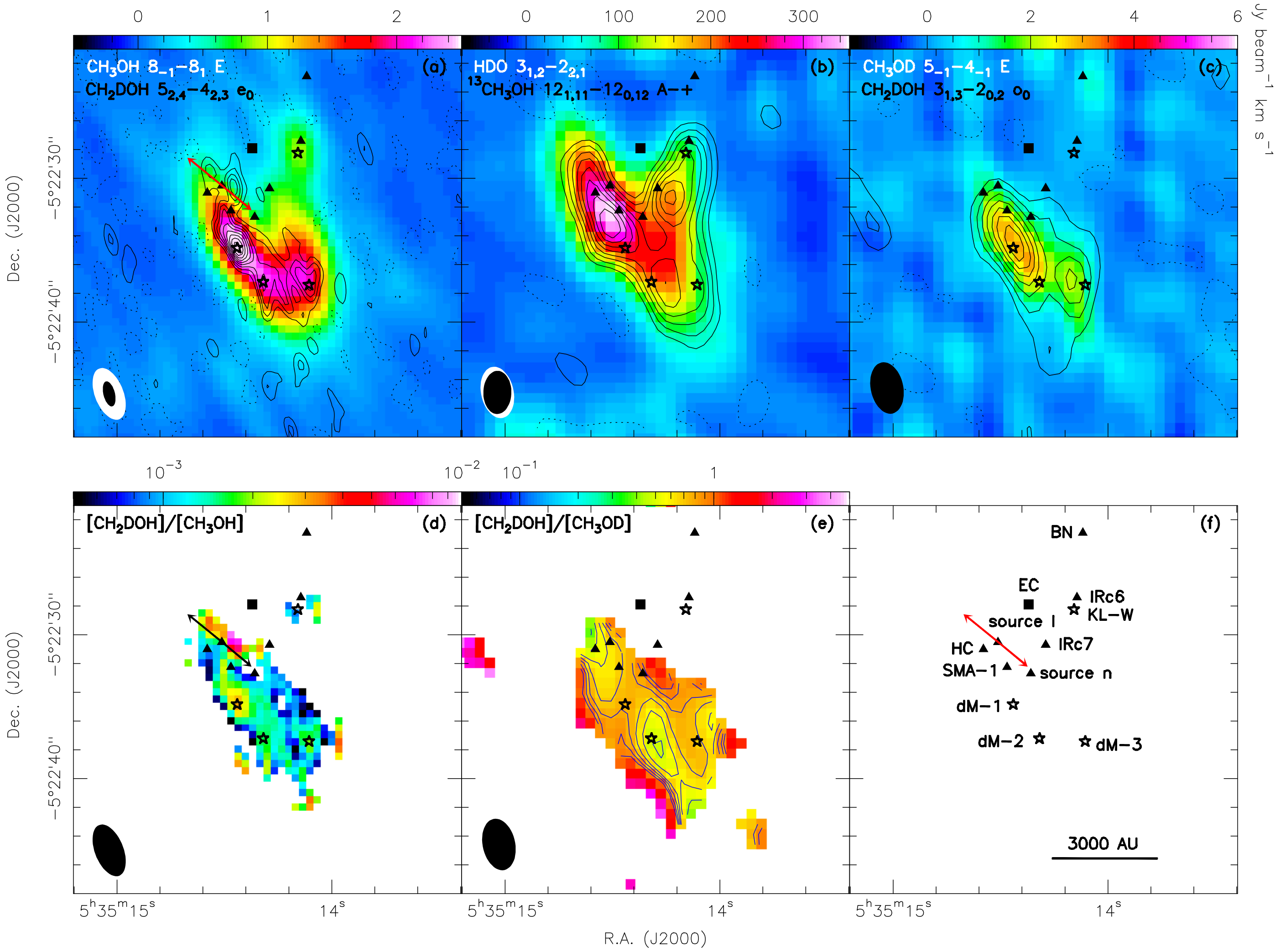

Fig. 3. (a) Color image showing the integrated intensity map of the CH$_3$OH 8$_{-2}$ – 8$_1$ E line ($E_{\rm up}/k$ = 109.6 K, integrated from 5 to 11 km s^{-1}) for a synthesized beam of 3.″8 × 2.″0. Black contours represent the CH$_2$DOH 5$_{2,4}$ – 4$_{2,3}$ line emission ($E_{\rm up}/k$ = 48.4 K, integrated from 5 to 11 km s^{-1}) and run from 15% to 95% in steps of 10% of the peak intensity (1.0 Jy beam^{-1} km s^{-1}) for a synthesized beam of 1.″8 × 0.″8. Black dashed contours correspond to –5% of the peak intensity. (b) Color image showing the PdBI integrated intensity map of of the HDO 3$_{1,2}$ – 2$_{2,1}$ line ($E_{\rm up}/k$ = 167.6 K, integrated from –8 to +17 km s^{-1}) for a synthesized beam of 3.″6 × 2.″3. Black contours represent the SMA ^{13}CH$_3$OH 12$_{1,11}$ – 12$_{0,12}$ A–+ emission ($E_{\rm up}/k$ = 192.8 K, integrated from 0 to 12 km s^{-1}, Y.-W. Tang, priv. comm.), running from 20% to 90% in steps of 10% of the peak intensity (316.6 Jy beam^{-1} km s^{-1}) for a synthesized beam of 3.″0 × 2.″0. Black dashed contours correspond to –10% of the peak intensity. (c) Integrated intensity map of the CH$_3$OD 5$_{-1}$ – 4$_{-1}$ E line ($E_{\rm up}/k$ = 37.3 K, from 5 to 11 km s^{-1}) overlaid with the CH$_2$DOH 3$_{1,2}$ – 2$_{0,2}$ o_0 line ($E_{\rm up}/k$ = 35.7 K, integrated from 5 to 11 km s^{-1}) in black contours for a synthesized beam of 3.″6 × 2.″3. Black contours run from 0.28 (2 σ) to 1.12 Jy beam^{-1} km s^{-1} in steps of 0.14 Jy beam^{-1} km s^{-1}, and black dashed contours correspond to −0.07 Jy beam^{-1} km s^{-1}. (d) [CH$_2$DOH]/[CH$_3$OH] abundance ratio map for a resolution of 3.″8 × 2.″0. The [CH$_2$DOH]/[CH$_3$OD] abundance ratio is calculated by assuming the same excitation temperature (120 K) for both molecules. (e) [CH$_2$DOH]/[CH$_3$OD] abundance ratio map for a resolution of 3.″6 × 2.″3. The [CH$_2$DOH]/[CH$_3$OD] abundance ratio is calculated by assuming the same excitation temperature (120 K) for both CH$_2$DOH and CH$_3$OD. Blue contours run from 0.4 to 1.0 in steps of 0.1. (f) The black square marks the center of explosion according to Zapata et al. (2009). The positions of source BN, the Hot Core (HC), IRc6/7, and source *I*/n, and SMA-1 are marked by triangles. The positions of deuterated methanol emission peaks (dM-1, dM-2, and dM-3) and KL-W are marked by stars. The bipolar outflow of source *I* is indicated.

Herschel may also be partly filtered out in our interferometric data.

Our three CH$_3$OH 101 GHz transitions include upper energy levels with $E_{\rm up}/k \lesssim 110$ K, from which we derived $T_{\rm rot}$ = 40−70 K. The CH$_3$OH lines in this energy level range detected by *Herschel* (see, e.g., Figure 4 in Wang et al., 2011) also give a similar trend: a low rotational temperature and a high column density are derived by using only the low $E_{\rm up}$ data in the CH$_3$OH population diagram. The CH$_3$OH lines from the *Herschel*/HIFI observations are optically thick, but the ^{13}CH$_3$OH lines (τ = 0.03−0.28) also show the same trend. This suggests that our low-temperature result ($T_{\rm rot}$ = 40 – 70 K) is unlikely to be caused by optical depth effects. Because the LSR velocities of our CH$_3$OH lines are consistent with the *Herschel*/HIFI data, it is more likely

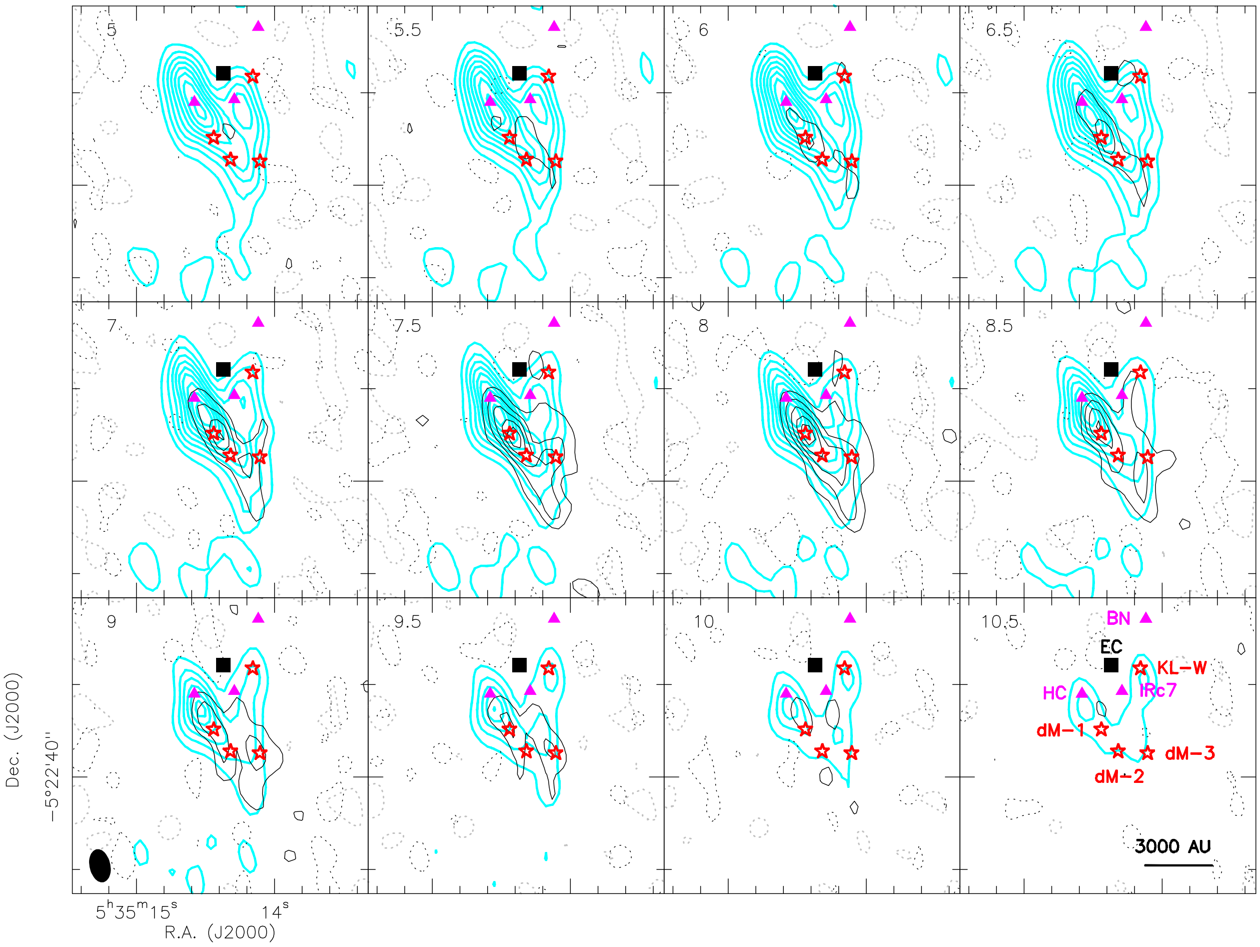

Fig. 4. Channel maps of the CH_2DOH emission at 225878.3 MHz (E_{up}/k = 35.7 K) in black contours overlaid with the HDO $3_{1,2} - 2_{2,1}$ line (E_{up}/k = 167.6 K) at 225896.7 MHz in light-blue contours for a synthesized beam of $3\farcs6 \times 2\farcs3$. The HDO emission contours run from 10% to 90% in steps of 10% of the peak intensity (17.9 Jy beam^{-1}), and the dashed contours represent –0.2 Jy beam^{-1} (5 σ). The CH_2DOH emission contours run from 0.08 to 0.48 Jy beam^{-1} in steps of 0.08 Jy beam^{-1}, and the black dashed contours represent –0.04 Jy beam^{-1} (1 σ). The black square marks the explosion center according to Zapata et al. (2009). The positions of source BN, the Hot Core (HC), and IRc7 are marked by magenta triangles, and the positions of the deuterated methanol emission peaks (dM-1, dM-2, and dM-3) are marked by red stars.

that our low CH_3OH excitation temperatures are not caused by a cold component along the line of sight, but that they are largely generated by subthermal excitation conditions.

4.4. Comparison with the HDO emission

In Figure 4, the superposition of HDO $3_{1,2} - 2_{2,1}$ and CH_2DOH $3_{1,3} - 2_{0,2}$ lines shows a globally similar distribution for different velocity channels. This result is significant because both lines were detected in the same PDBI data set around 225.9 GHz. However, details differ, as one may expect for two transitions with different upper energy levels (168 K and 36 K for HDO and CH_2DOH, respectively), and for different molecular formation scenarios, which imply, for instance, that methanol is formed on grain surfaces at higher densities than water.

The HDO emission peaks between the Orion Hot Core and dM-1, near the dust clump SMA-1 (Beuther et al., 2004, ; see also our Fig. 3). Dust emission toward this peak has been detected with SMA in the 870 μm band by Tang et al. (2010). Owing to a position offset of about 1′′, it is not clear whether this clump coincides with the SMA-1 position observed by Beuther et al. (2004) with a resolution of $0\farcs78 \times 0\farcs65$. In addition to the prominent emission peak near SMA-1, the HDO emission shows a similar V-shaped distribution as CH_3OH. There is HDO emission close to the IR source IRc7, but it is interesting to note that the HDO emission does not peak at IRc7. It peaks to the southwest of IRc7 instead. A similar situation is observed with SMA for the $^{13}CH_3OH$ emission (see the right panel of Figure 3; Y.-W. Tang, priv. comm.). In addition, it seems that the overall CH_2DOH emission distribution is shifted to the south by a few arcseconds with respect to the HDO emission. For example, the strongest HDO emission peak, which corresponds to the NH_3 column density peak derived by Goddi et al. (2011), is located 3′′ north of dM-1. This shift is clearly seen in Figure 3 where the HDO and $^{13}CH_3OH$ emissions lie farther north than the CH_3OH and CH_2DOH emissions. The different spatial distributions observed for CH_2DOH and CH_3OH on one side, and HDO and $^{13}CH_3OH$ on the other side (see Figs. 3 and 4) cannot be attributed to optical depth effects because (a) we have shown that our CH_2DOH (1.3 mm emission) and CH_3OH (3 mm emission) data are optically thin; (b) our estimate of the HDO line opacity is $\lesssim$ 0.3 (agrees with Jacq et al., 1990). The difference observed in the distribution of these molecular species could be due to different temperatures across the Orion molecular material involving processes such as heating by luminous infrared sources or shocks.

4.5. Deuteration ratios of water and methanol

The [HDO]/[H_2O] abundance ratio has been reported to be about a few times 10^{-4} toward Orion BN/KL (see, e.g., Pardo et al., 2001; Jacq et al., 1990), which is about one order of magnitude lower than the [CH_2DOH]/[CH_3OH] ratio derived here. [HDO]/[H_2O] ratios lower than the [CH_2DOH]/[CH_3OH] ratios have also been reported toward low-mass protostars (Parise et al., 2005; Liu et al., 2011). Since heavy water (D_2O) is much less abundant than HDO, i.e., [D_2O]/[HDO]=1.7×10^{-3} in IRAS 16293–2422 (Butner et al., 2007), HDO seems to be the main deuterium (gas phase) reservoir for water in Orion BN/KL. For methanol, CH_3OD is as abundant as CH_2DOH, and other doubly or multiply deuterated methanol species are expected to be less abundant. Therefore, the total deuteration ratio for methanol (including CH_2DOH and CH_3OD) in Orion BN/KL is about one order of magnitude higher than that of water (including HDO and D_2O). If both water and methanol sublimate from ice mantles with similar time scales, and supposing that their destruction rates are comparable, the higher abundance of deuterated methanol may just reflect different chemical reaction speeds on dust surface. At a later stage, formation and destruction rates in the gas phase will of course complicate the analysis. Some experiments have been conducted to investigate this question. For example, H-D exchange between water and methanol has been proposed by several authors in different physical conditions, e.g., temperature increase and ultraviolet light irradiation (Ratajczak et al., 2009; Weber et al., 2009). In addition, the enrichment of deuterated methanol has been experimentally reproduced by H-D substitution in solid methanol at 10 K. However, a high atomic D/H ratio of 0.1 was required and the substitution was not seen in water and ammonia (Nagaoka et al., 2005). Therefore, H-D substitution may qualitatively explain why methanol is easier to be deuterated than water; but more chemical experiments and modeling are clearly needed to quantitatively address this question.

5. Conclusions

The main findings and conclusions of our study based on observations of several transitions of deuterated methanol and one transition of deuterated water in Orion BN/KL are as follows.

1. We have obtained the first high angular resolution ($1\farcs8\times0\farcs8$) CH_2DOH images detected around 223.5 GHz toward Orion BN/KL and compared these data with somewhat lower resolution ($3\farcs8\times2\farcs0$) CH_3OH images at 101.5 GHz. The strongest CH_2DOH and CH_3OH emissions come from the Hot Core southwest region exhibiting an LSR velocity of about 8 km s^{-1}, typical of the Orion Compact Ridge region. The CH_2DOH emission is clumpy and the column densities are estimated to be about $1-9\times10^{15}$ cm^{-2} toward these clumps. The CH_3OH column densities are about $3-5\times10^{17}$ cm^{-2} across Orion BN/KL, leading to a [CH_2DOH]/[CH_3OH] deuteration ratio of $0.8-1.3\times10^{-3}$ toward three deuterated methanol clumps and below 2×10^{-4} toward KL-W.
2. The [CH_2DOH]/[CH_3OD] abundance ratio map was obtained for Orion BN/KL, and their ratios are less than unity at the central part of the region. These ratios are lower than the statistical factor of 3 derived in the simplest deuteration models, and definitely lower than the values derived in low-mass protostars (e.g., Parise et al., 2002; Ratajczak et al., 2011).
3. We have mapped with moderately high spatial resolution ($3\farcs6\times2\farcs3$) the 225.9 GHz transition of HDO and compared its distribution with CH_2DOH, CH_3OH, and $^{13}CH_3OH$. We find that the deuterated water ratio is about one order of magnitude lower than the deuterated methanol ratio. H-D substitution may explain why methanol is easier to be deuterated than water.
4. The deuteration ratios derived in this work are not strongly different from one clump to another, except perhaps toward KL-W where more observations are desirable to conclude. However, to explain the slight differences observed locally in the abundance ratios of identified clumps, we suggest that various processes could be competing, for instance, heating by luminous infrared sources, or heating by shocks.

Acknowledgements. We thank Y.-W. Tang for kindly providing the SMA $^{13}CH_3OH$ image. T.-C. Peng acknowledges support from the ALMA grant 2009-18 at Université de Bordeaux1/LAB. B. Parise is supported by the German Deutsche Forschungsgemeinschaft, DFG Emmy Noether project number PA1692/1-1. We thank the referee, who helped us in restructuring our initial work and in clarifying our main conclusions.

References

Anderson, T., Crownover, R. L., Herbst, E., & De Lucia, F. C. 1988, ApJS, 67, 135
Becklin, E. E., & Neugebauer, G. 1967, ApJ, 147, 799
Beuther, H., et al. 2004, ApJ, 616, L31
Beuther, H., et al. 2005, ApJ, 632, 355
Blake, G. A., Sutton, E. C., Masson, C. R., & Phillips, T. G. 1987, ApJ, 315, 621
Butner, H. M., Charnley, S. B., Ceccarelli, C., Rodgers, S. D., Pardo, J. R., Parise, B., Cernicharo, J., & Davis, G. R. 2007, ApJ, 659, L137
Charnley, S. B., Tielens, A. G. G. M., & Rodgers, S. D. 1997, ApJ, 482, L203
Clark, B. G. 1980, A&A, 89, 377
Chandler, C. J., & Wood, D. O. S. 1997, MNRAS, 287, 445
Downes, D., Genzel, R., Becklin, E. E., & Wynn-Williams, C. G. 1981, ApJ, 244, 869
Favre, C., Despois, D., Brouillet, N., Baudry, A., Combes, F., Guélin, M., Wootten, A., & Wlodarczak, G. 2011, A&A, 532, A32
Friedel, D. N., & Snyder, L. E. 2008, ApJ, 672, 962
Garay, G., Moran, J. M., & Reid, M. J. 1987, ApJ, 314, 535
Gezari, D. Y. 1992, ApJ, 396, L43
Gezari, D. Y., Backman, D. E., & Werner, M. W. 1998, ApJ, 509, 283
Goddi, C., Greenhill, L. J., Humphreys, E. M. L., Chandler, C. J., & Matthews, L. D. 2011, ApJ, 739, L13
Goldsmith, P. F., & Langer, W. D. 1999, ApJ, 517, 209
Ivash, E. V., & Dennison, D. M. 1953, J. Chem. Phys., 21, 1804
Jacq, T., Walmsley, C. M., Henkel, C., Baudry, A., Mauersberger, R., & Jewell, P. R. 1990, A&A, 228, 447
Jacq, T., Walmsley, C. M., Mauersberger, R., Anderson, T., Herbst, E., & De Lucia, F. C. 1993, A&A, 271, 276
Kleinmann, D. E., & Low, F. J. 1967, ApJ, 149, L1
Lauvergnat, D., Coudert, L. H., Klee, S., & Smirnov, M. 2009, Journal of Molecular Spectroscopy, 256, 204
Linsky, J. L., et al. 2006, ApJ, 647, 1106
Lis, D. C., Roueff, E., Gerin, M., Phillips, T. G., Coudert, L. H., van der Tak, F. F. S., & Schilke, P. 2002, ApJ, 571, L55
Liu, F.-C., Parise, B., Kristensen, L., Visser, R., van Dishoeck, E. F., Güsten, R. 2011, A&A, 527, A19
Matsakis, D. N., Wright, M. C. H., Townes, C. H., Welch, W. J., Cheung, A. C., & Askne, J. I. H. 1980, ApJ, 236, 481
Mauersberger, R., Henkel, C., Jacq, T., & Walmsley, C. M. 1988, A&A, 194, L1
Menten, K. M., Walmsley, C. M., Henkel, C., & Wilson, T. L. 1988, A&A, 198, 253
Menten, K. M., & Reid, M. J. 1995, ApJ, 445, L157
Menten, K. M., Reid, M. J., Forbrich, J., & Brunthaler, A. 2007, A&A, 474, 515
Mukhopadhyay, I., Perry, D. S., Duan, Y.-B., Pearson, J. C., Albert, S., Butler, R. A. H., Herbst, E., & De Lucia, F. C. 2002, J. Chem. Phys., 116, 3710
Nagaoka, A., Watanabe, N., & Kouchi, A. 2005, ApJ, 624, L29
Neill, J. L., et al. 2011, Journal of Physical Chemistry A, 115, 6472

Osamura, Y., Roberts, H., & Herbst, E. 2004, A&A, 421, 1101
Pardo, J. R., Cernicharo, J., Herpin, F., Kawamura, J., Kooi, J., & Phillips, T. G. 2001, ApJ, 562, 799
Parise, B., et al. 2002, A&A, 393, L49
Parise, B., Castets, A., Herbst, E., Caux, E., Ceccarelli, C., Mukhopadhyay, I., & Tielens, A. G. G. M. 2004, A&A, 416, 159
Parise, B., et al. 2005, A&A, 431, 547
Parise, B., Ceccarelli, C., Tielens, A. G. G. M., Castets, A., Caux, E., Lefloch, B., & Maret, S. 2006, A&A, 453, 949
Pearson, J. C., Sastry, K. V. L. N., Herbst, E., & De Lucia, F. C. 1997, ApJ, 480, 420
Peng, T.-C., Wyrowski, F., Zapata, L. A., Güsten, R., & Menten, K. M. 2012, A&A, 538, A12
Plambeck, R. L., & Wright, M. C. H. 1988, ApJ, 330, L61
Ratajczak, A., Quirico, E., Faure, A., Schmitt, B., & Ceccarelli, C. 2009, A&A, 496, L21
Ratajczak, A., Taquet, V., Kahane, C., Ceccarelli, C., Faure, A., & Quirico, E. 2011, A&A, 528, L13
Rieke, G. H., Low, F. J., & Kleinmann, D. E. 1973, ApJ, 186, L7
Roberts, H., & Millar, T. J. 2000, A&A, 361, 388
Roberts, H., Herbst, E., & Millar, T. J. 2003, ApJ, 591, L41
Rodgers, S. D., & Charnley, S. B. 2002, Planet. Space Sci., 50, 1125
Rodriguez Kuiper, E. N., Kuiper, T. B. H., & Zuckerman, B. 1978, ApJ, 219, L49
Tang, Y.-W., Ho, P. T. P., Koch, P. M., & Rao, R. 2010, ApJ, 717, 1262
Turner, B. E., Fourikis, N., Morris, M., Palmer, P., & Zuckerman, B. 1975, ApJ, 198, L125
Turner, B. E. 1990, ApJ, 362, L29
Turner, B. E. 1991, ApJS, 76, 617
van der Tak, F. F. S., Schilke, P., Müller, H. S. P., Lis, D. C., Phillips, T. G., Gerin, M., & Roueff, E. 2002, A&A, 388, L53
Wang, K.-S., Kuan, Y.-J., Liu, S.-Y., & Charnley, S. B. 2010, ApJ, 713, 1192
Wang, S., et al. 2011, A&A, 527, A95
Weber, A. S., Hodyss, R., Johnson, P. V., Willacy, K., & Kanik, I. 2009, ApJ, 703, 1030
Wright, M., Sandell, G., Wilner, D. J., & Plambeck, R. L. 1992, ApJ, 393, 225
Wright, M. C. H., Plambeck, R. L., & Wilner, D. J. 1996, ApJ, 469, 216
Xu, L.-H., et al. 2008, Journal of Molecular Spectroscopy, 251, 305
Zapata, L. A., Schmid-Burgk, J., Ho, P. T. P., Rodríguez, L. F., & Menten, K. M. 2009, ApJ, 704, L45
Zapata, L. A., Schmid-Burgk, J., & Menten, K. M. 2011, A&A, 529, A24

Appendix A: Revisiting the CH_2DOH/CH_3OD abundance ratios in Orion BN/KL

To compare our high angular resolution data with previous single-dish observations, we re-calculated the temperatures and column densities obtained by Mauersberger et al. (1988) and Jacq et al. (1993) from their 30m data for CH_3OD and CH_2DOH, respectively. The line parameters of CH_3OD and CH_2DOH used in the calculations are listed in Table A.1, and the population diagrams are shown in Figure A.1.

CH_3OD

We selected only five clean CH_3OD lines (without any apparent line-blending) around 140–156 GHz detected by Mauersberger et al. (1988) with a similar resolution of 16″–17″ to reduce the fitting uncertainty. The CH_3OD lines detected by Jacq et al. (1993) were excluded because no CH_3OD spectra can be used to judge the possible line-blending and data quality. Effective line strengths $S\mu^2$ of the CH_3OD lines were taken from Anderson et al. (1988), and the partition function $Q = 1.41\ T^{1.5}$ was used. The rotational temperature (132.4±19.6 K) and column density ($4.4 \pm 0.3 \times 10^{15}$ cm^{-2}) were estimated by a least-squares fit (Fig. A.1), assuming a source size of 15″. The revised CH_3OD temperature and column density are consistent with those of Mauersberger et al. (1988), who derived a rotational temperature of 50–150 K and a column density of $1 - 5 \times 10^{15}$ cm^{-2}.

CH_2DOH

For CH_2DOH, we judge that only the three detections reported by Jacq et al. (1993) can be reliably used in the population diagrams (see Table A.1). Both old CH_2DOH $S\mu^2$ values taken from Jacq et al. (1993) and new ones (see Table A.1) provided by B. Parise (priv. comm.) were used in the calculations. (Fig. A.1). The CH_2DOH partition function $Q = 2.25\ T^{1.5}$ and a source size of 15″ were used here.

The new values of CH_2DOH $S\mu^2$ employed in this work are based on those tabulated in the paper by Parise et al. (2002) but a factor of three higher. This revision corrects for an inconsistency with the partition function reported by Parise et al. (2002), and some dipole moment values can be quite uncertain, which may explain the discrepancy with the values used by Jacq et al. (1993) and why they were never officially released in the JPL database. However, as shown below, both the old $S\mu^2$ values used by Jacq et al. (1993) and new ones adopted here give similar estimates of the CH_2DOH column densities in Orion BN/KL. We believe that the uncertainties of the CH_2DOH $S\mu^2$ values of our present work are not dominant in the column density calculations. Nevertheless, a new spectroscopic study of CH_2DOH with a robust fitting of the Hamiltonian would definitely give better confidence in these intensities.

Using the old $S\mu^2$, a least-squares fit to the CH_2DOH data shows a low rotational temperature (about 25±10 K) with a column density of 5.0×10^{14} cm^{-2}, consistent with the first estimate of Jacq et al. (1993), who derived a rotational temperature of 34^{+60}_{-13} K and a column density of $6{\times}10^{14}$ cm^{-2}. However, since the rotational temperatures derived by Menten et al. (1988) and Mauersberger et al. (1988) for CH_3OH and CH_3OD are about 100 K toward Orion BN/KL, Jacq et al. (1993) also adopted a higher temperature for CH_2DOH. They obtained a CH_2DOH column density of 3.9×10^{15} cm^{-2}, which is 2.6 times higher than our revised value (1.6×10^{15} cm^{-2}, see Fig. A.1 upper panel). This is because they appear to correct the beam-filling factor twice in their N_l/g_l calculations and population diagram. Therefore, the CH_2DOH column density derived by Jacq et al. (1993) with a temperature of 100 K was overestimated by a factor of 2–3.

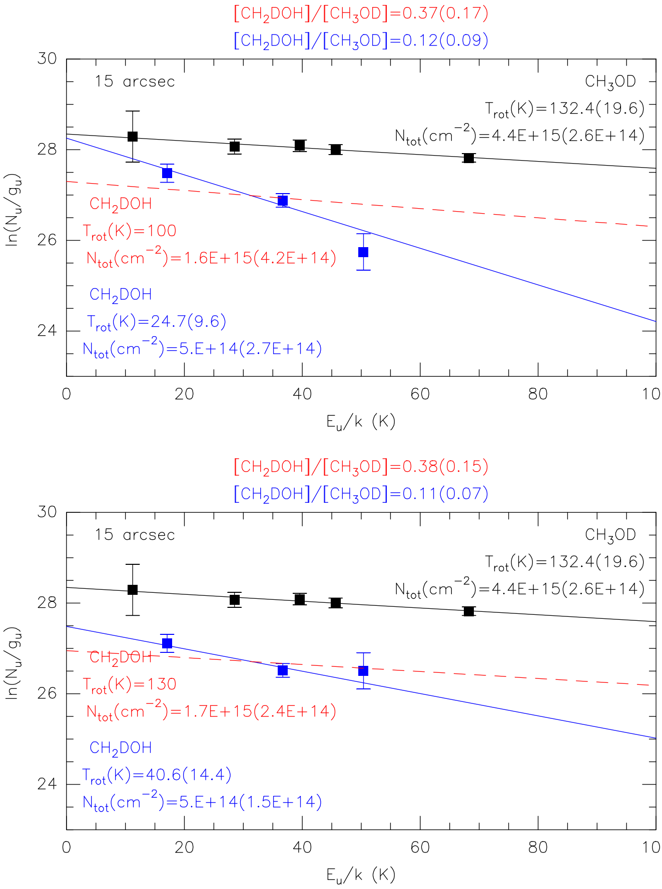

Fig. A.1. Population diagrams of CH_3OD and CH_2DOH using the 30m data of Mauersberger et al. (1988) and Jacq et al. (1993), respectively. The old CH_2DOH effective line strengths of Jacq et al. (1993) (upper panel) and the new ones (lower panel) were used in the calculations. The beam filling factor was taken into account by assuming a source size of 15″. The rotational temperatures and column densities were estimated by a least-squares fit, and the results and uncertainties are given in the diagrams. For CH_2DOH, the red dashed line in the upper panel indicates the fit with a fixed temperature of 100 K as adopted by Jacq et al. (1993) and the one in the lower panel the fit with a temperature of 130 K (the same as the CH_3OD temperature derived here).

With the new CH_2DOH $S\mu^2$, we derive a somewhat higher rotational temperature (40.6 ± 14.4 K) and a column density of 5.0×10^{14} cm^{-2} similar to that derived by using the old $S\mu^2$. This suggests that the uncertainties in the CH_2DOH effective line strengths do not strongly affect the CH_2DOH column density estimate in this case.

CH_2DOH/CH_3OD abundance ratios

The overestimated CH_2DOH column density derived by Jacq et al. (1993) leads to a higher $[CH_2DOH]/[CH_3OD]$ abundance ratio (1.1–1.5) toward IRc2. The new calculation indicates that the $[CH_2DOH]/[CH_3OD]$ abundance ratio is 0.2–0.5 with a source size of 15″, assuming CH_2DOH and CH_3OD have the same temperature of about 130 K. For a lower CH_2DOH temperature (i.e., about 40 K), the [CH_2DOH]/[CH_3OD] ratio is even lower (about 0.1).

In addition, the CH_3OD data of Mauersberger et al. (1988) were taken at the position close to KL-W (KL-W_M hereafter, Menten et al., 1988) instead of IRc2, which was used as the central position by Jacq et al. (1993). According to our CH_3OD image (Fig. 3), the intensity observed toward IRc2 is about twice as high as that of KL-W_M, assuming a 30m telescope beam size of about 18″ at 140 GHz and the same filtering. Therefore, the CH_3OD abundance in Orion BN/KL derived by Mauersberger et al. (1988) may be underestimated by 50% at most. A similar calculation (Fig. B.5) also shows that the CH_3OH column density toward KL-W_M is about 20% lower than that toward IRc2.

In short, we conclude that the revisited [CH_2DOH]/[CH_3OD] abundance ratio derived from the previous 30m observations is $\lesssim 0.6$, and the [CH_2DOH]/[CH_3OH] abundance ratio is estimated to be $0.8 - 2.8 \times 10^{-3}$ toward IRc2, by adopting a CH_3OH column density of $4.7 \pm 0.3 \times 10^{17}$ cm^{-2} (Menten et al., 1988) and correcting the possible density underestimate of about 20% toward IRc2 (for a source size of 15″).

Appendix B: Complementary figures and tables

Table A.1. 30m CH_3OD and CH_2DOH line parameters

Frequency (MHz)	Transition (J_{k_a,k_c})	$E_{\rm up}/k$ (K)	$S\mu^2$ (D^2)	$\int T_{\rm MB} dV$ (K km s^{-1})	f^c	$N_{\rm u}/g_{\rm u}{}^d$ (cm^{-2})	Comment
				CH_3OD [a]			
140175.20	$4_{1,3} - 4_{0,4}$ A−−	19.8	9.3	5.1 ± 0.7	0.42	$1.55 \pm 0.25 \times 10^{12}$	
143741.65	$5_{1,4} - 5_{0,5}$ A−−	27.5	11.2	6.6 ± 0.7	0.43	$1.57 \pm 0.20 \times 10^{12}$	
148359.77	$6_{0,6} - 5_{1,5}$ A++	31.7	5.7	3.3 ± 0.3	0.45	$1.45 \pm 0.16 \times 10^{12}$	
153324.00	$7_{1,6} - 7_{0,7}$ A−−	47.4	14.7	7.6 ± 0.6	0.47	$1.21 \pm 0.11 \times 10^{12}$	
155533.08	$1_{1,0} - 0_{0,0}$ E	7.8	1.0	0.9 ± 0.4	0.47	$1.93 \pm 1.09 \times 10^{12}$	
				CH_2DOH [b]			
99672.23	$6_{1,5} - 6_{0,6}$ e_0	50.4	12.3[e]	0.3 ± 0.1	0.27	$1.51 \pm 0.61 \times 10^{11}$	
136151.26	$3_{1,2} - 2_{1,1}$ e_0	17.1	2.1[e]	0.6 ± 0.1	0.41	$8.58 \pm 1.72 \times 10^{11}$	[g]
226818.36	$5_{1,4} - 4_{1,3}$ e_0	36.7	3.8[e]	1.6 ± 0.2	0.66	$4.72 \pm 0.71 \times 10^{11}$	[g]
99672.23	$6_{1,5} - 6_{0,6}$ e_0	50.4	5.8[f]	0.3 ± 0.1	0.27	$3.23 \pm 1.29 \times 10^{11}$	
136151.26	$3_{1,2} - 2_{1,1}$ e_0	17.1	3.1[f]	0.6 ± 0.1	0.41	$5.91 \pm 1.18 \times 10^{11}$	[g]
226818.36	$5_{1,4} - 4_{1,3}$ e_0	36.7	5.5[f]	1.6 ± 0.2	0.66	$3.27 \pm 0.49 \times 10^{11}$	[g]

Notes. [a] Mauersberger et al. (1988); centered at KL-W_M ($05^h35^m14\overset{s}{.}18$, $-05°22'26\overset{''}{.}5$, J2000). [b] Jacq et al. (1993); centered at IRc2 ($05^h35^m14\overset{s}{.}47$, $-05°22'30\overset{''}{.}2$, J2000). [c] The beam filling factor $f = \theta_s^2/(\theta_s^2 + \theta_b^2)$ is calculated by assuming a source size θ_s of 15″. θ_b is the 30m beam size. [d] The beam filling factor is taken into account in the calculation of N_u, and the rms noise and calibration uncertainties are included (assuming 20%). [e] The Old $S\mu^2$ taken from Jacq et al. (1993) [f] The New $S\mu^2$ provided by B. Parise (priv. comm.). [g] The data obtained at the offset position (0″,−6″) of IRc2.

Table B.1. PdBI CH_2DOH line parameters at dM-1, dM-2, and dM-3

Frequency[a] (MHz)	Transition (J_{k_a,k_c})	$E_{\rm up}/k$ (K)	$S\mu^2$ (D^2)	$T_{\rm peak}$ (K)	$V_{\rm LSR}$ (km s^{-1})	ΔV (km s^{-1})	$\int T dV$ (K km s^{-1})	Comment
				dM-1				
105806.4100	$11_{1,10} - 11_{0,11}$ e_1	159.4	6.11	0.45 ± 0.02	7.81 ± 0.89	2.85 ± 1.09	1.23 ± 0.05	blended[c]
223422.2629	$5_{2,4} - 4_{2,3}$ e_0	48.4	5.15	4.77 ± 0.35	7.96 ± 0.84	2.71 ± 1.14	14.29 ± 0.50	
223616.1420	$5_{4,2} - 4_{4,1}$, $5_{4,1} - 4_{4,0}$ e_0	95.2	2.15[b]	2.91 ± 0.35	7.70 ± 0.84	2.78 ± 2.14	6.95 ± 0.23	
223691.5380	$5_{3,3} - 4_{3,2}$ e_0	68.2	3.96	4.81 ± 0.35	6.99 ± 0.84	2.78 ± 1.68	15.87 ± 1.76	blended[d]
223697.1880	$5_{3,2} - 4_{3,1}$ e_0	68.2	3.96	3.04 ± 0.35	7.79 ± 0.84	1.64 ± 1.35	6.17 ± 1.03	blended[e]
225878.2540	$3_{1,3} - 2_{0,2}$ o_0	35.7	2.28	1.27 ± 0.12	7.75 ± 0.42	2.67 ± 0.44	3.10 ± 0.20	
				dM-2				
105806.4100	$11_{1,10} - 11_{0,11}$ e_1	159.4	6.11	0.38 ± 0.02	7.81 ± 0.89	2.91 ± 1.07	1.02 ± 0.05	
223422.2629	$5_{2,4} - 4_{2,3}$ e_0	48.4	5.15	2.79 ± 0.35	7.96 ± 0.84	1.83 ± 0.54	5.19 ± 0.48	
223616.1420	$5_{4,2} - 4_{4,1}$, $5_{4,1} - 4_{4,0}$ e_0	95.2	2.15[b]	1.22 ± 0.35	7.30 ± 0.84	2.84 ± 1.33	3.03 ± 0.32	
223691.5380	$5_{3,3} - 4_{3,2}$ e_0	68.2	3.96	1.40 ± 0.35	7.79 ± 0.84	2.80 ± 1.68	2.43 ± 0.55	blended[d]
223697.1880	$5_{3,2} - 4_{3,1}$ e_0	68.2	3.96	0.68 ± 0.35	7.86 ± 0.84	1.22 ± 0.97	1.89 ± 0.55	
225878.2540	$3_{1,3} - 2_{0,2}$ o_0	35.7	2.28	1.07 ± 0.12	7.76 ± 0.42	2.52 ± 0.42	2.29 ± 0.19	
				dM-3				
105806.4100	$11_{1,10} - 11_{0,11}$ e_1	159.4	6.11	0.32 ± 0.02	7.89 ± 0.89	3.36 ± 0.89	1.02 ± 0.05	
223422.2629	$5_{2,4} - 4_{2,3}$ e_0	48.4	5.15	0.76 ± 0.35	7.92 ± 0.84	...	2.87 ± 1.35	
223616.1420	$5_{4,2} - 4_{4,1}$, $5_{4,1} - 4_{4,0}$ e_0	95.2	2.15[b]	< 0.35	...	...	< 1.75	
223691.5380	$5_{3,3} - 4_{3,2}$ e_0	68.2	3.96	1.40 ± 0.35	7.76 ± 0.84	3.43 ± 0.90	4.23 ± 0.26	
223697.1880	$5_{3,2} - 4_{3,1}$ e_0	68.2	3.96	0.93 ± 0.35	7.84 ± 0.84	4.18 ± 1.05	3.43 ± 0.31	
225878.2540	$3_{1,3} - 2_{0,2}$ o_0	35.7	2.28	0.76 ± 0.12	7.71 ± 0.42	0.87 ± 0.45	0.71 ± 0.11	1st component
				0.66 ± 0.12	9.05 ± 0.42	1.22 ± 0.45	0.83 ± 0.18	2nd component

Notes. [a] Line frequencies of the detected lines [b] Effective line strengths of each single line [c] This line is blended with the $H^{13}CCCN$ $J = 12-11$ line at 105799.1130 MHz toward dM-1. [d] This line is blended with the U223694.8 line. [e] This line is blended with the U223694.3 line and the acetone line at 223692.1 MHz.

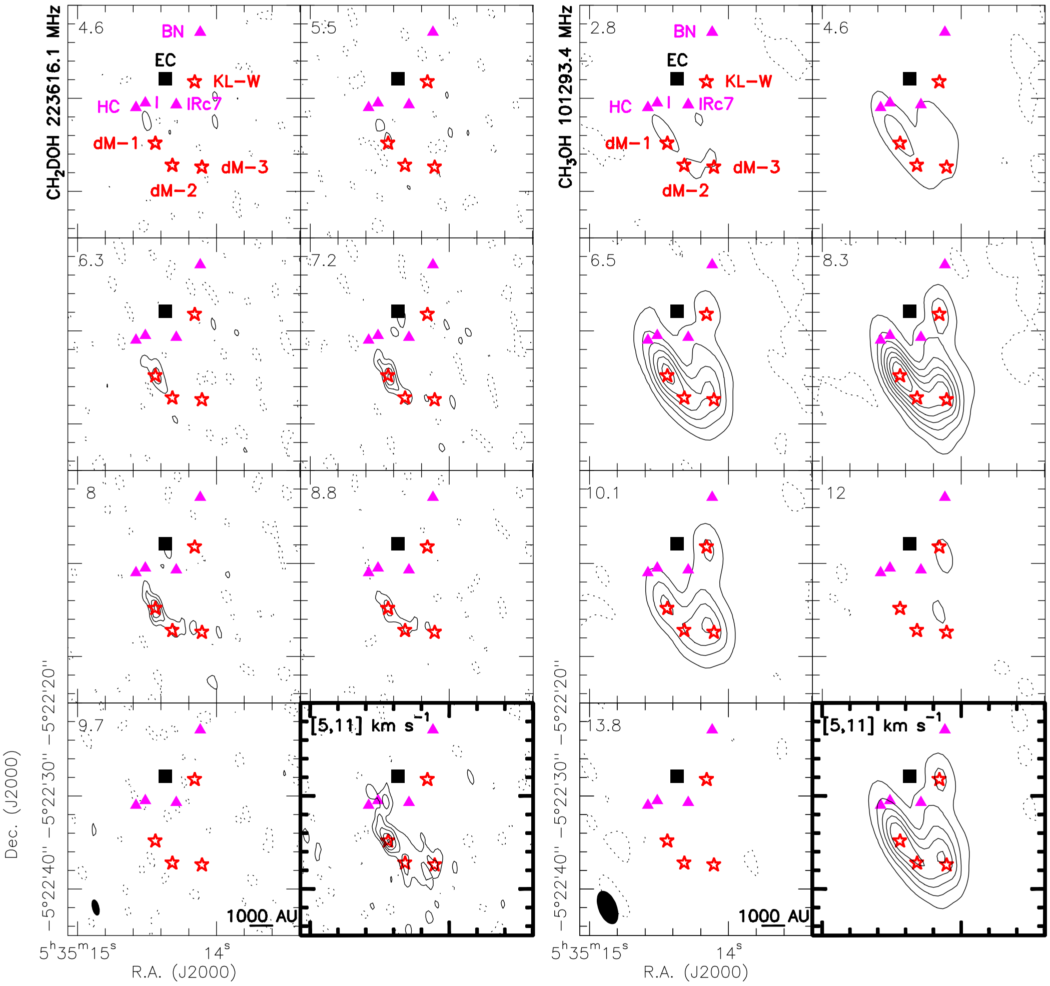

Fig. B.1. Left: Channel maps of the CH_2DOH doublet ($E_{\rm up}/k$ = 48.4 K) emission at 223616.1 MHz for a synthesized beam of 1.″8 × 0.″8. Contours run from 40 mJy beam^{-1} (2 σ) to 160 mJy beam^{-1} (2.77 K) in steps of 40 mJy beam^{-1}, and the dashed contours represent –20 mJy beam^{-1}. The bottom-right panel shows the integrated intensity (from 5 to 11 km s^{-1}) in contours running from 0.15 to 0.45 Jy beam^{-1} km s^{-1} in steps of 0.15 Jy beam^{-1} km s^{-1}, and the dashed contours represent –0.08 Jy beam^{-1} km s^{-1}. Right: Channel maps of the CH_3OH $7_{-2} - 7_1$ E ($E_{\rm up}/k$ = 91.0 K) emission at 101293.4 MHz for a synthesized beam of 3.″8 × 2.″0. Contours run from 50 to 350 mJy beam^{-1} in steps of 50 mJy beam^{-1}. The dashed contours represent –30 mJy beam^{-1}(1 σ). The bottom-right panel shows the integrated intensity of CH_3OH (from 5 to 11 km s^{-1}) in contours running from 0.3 to 1.5 Jy beam^{-1} km s^{-1} in steps of 0.3 Jy beam^{-1} km s^{-1}, and the dashed contours represent –0.03 Jy beam^{-1} km s^{-1}. The black square marks the center of explosion according to Zapata et al. (2009). The positions of source BN, the Hot Core (HC), IRc7, and source *I* are marked by triangles. The positions of deuterated methanol emission peaks (dM-1, dM-2, and dM-3) and KL-W are marked by red stars.

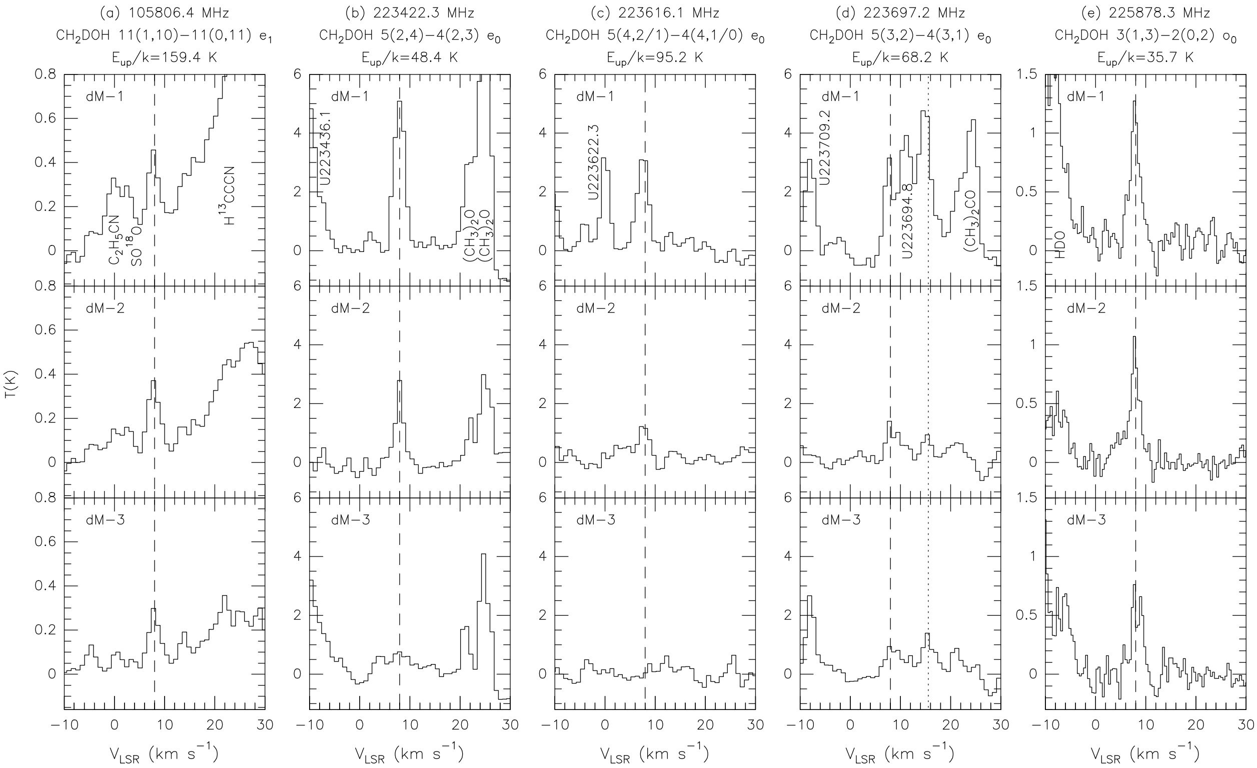

Fig. B.2. CH_2DOH spectra toward dM-1, dM-2, and dM-3 for a synthesized beam of $1\farcs8 \times 0\farcs8$. The dashed lines indicate a $V_{\rm LSR}$ of 8 km s^{-1}. The unidentified molecular lines are denoted with their frequencies. (a) For dM-1, the CH_2DOH $11_{1,10} - 11_{0,11}$ e_1 line is blended with a broad $H^{13}CCCN$ $J = 12 - 11$ line ($\Delta V \approx 10$ km s^{-1}) at 105799.1 MHz. The rms noise ($1\,\sigma$) is 0.02 K. (b)-(d) The dotted line indicates the CH_2DOH $5_{3,3} - 4_{3,2}$ e_0 line at 223691.5 MHz, which is blended with the $(CH_3)_2CO$ $17_{7,11} - 16_{6,10}$ EA/AE lines at 223692.1 MHz. The rms noise ($1\,\sigma$) is 0.35 K. (e) The strong line to the left is the HDO $3_{1,2} - 2_{2,1}$ line at 225896.7 MHz. Two velocity components at 7.8 and 9.0 km s^{-1} are seen toward dM-3. The rms noise ($1\,\sigma$) is 0.12 K.

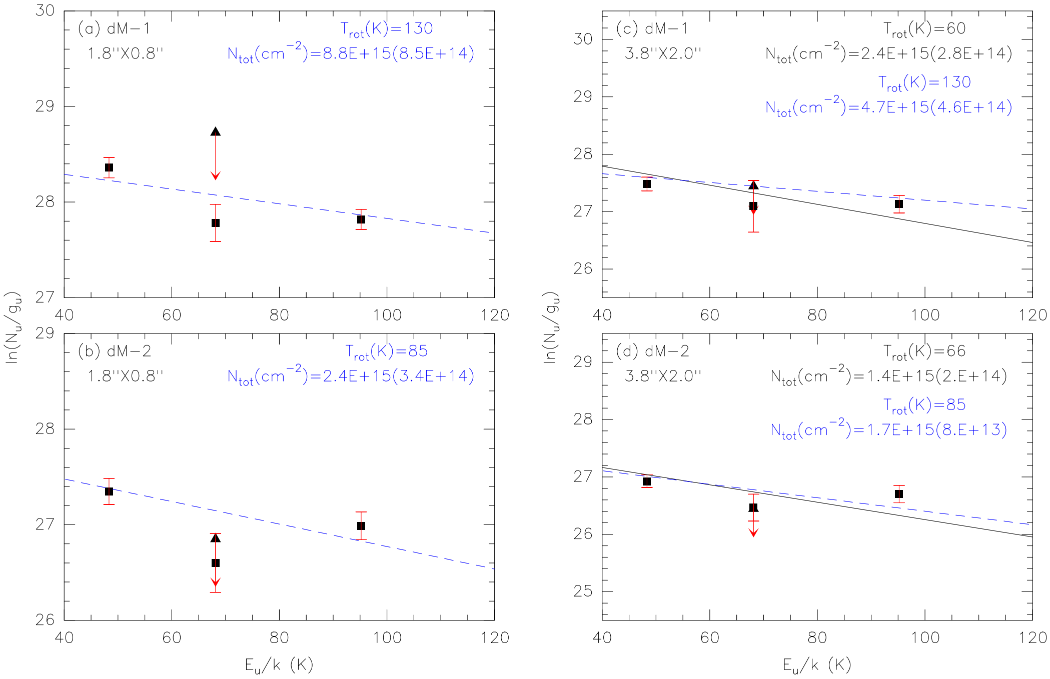

Fig. B.3. CH_2DOH population diagrams of dM-1 and dM-2. (a)–(b) Population diagrams of the high angular resolution data. The rotational temperatures are assumed to be 130 K and 85 K for dM-1 and dM-2, respectively. (c)–(d) Population diagrams for the data smoothed to a resolution of $3\farcs8 \times 2\farcs0$. Low rotational temperatures and higher ones are assumed to be 60 K and 130 K for dM-1 and 66 K and 85 K for dM-2, respectively. The fits of low temperatures are plotted in black lines and higher temperatures in blue dashed lines. The CH_2DOH column densities are estimated by a least-squares fit, where the uncertainties include the statistical error, the rms noise, and calibration uncertainties (10%).

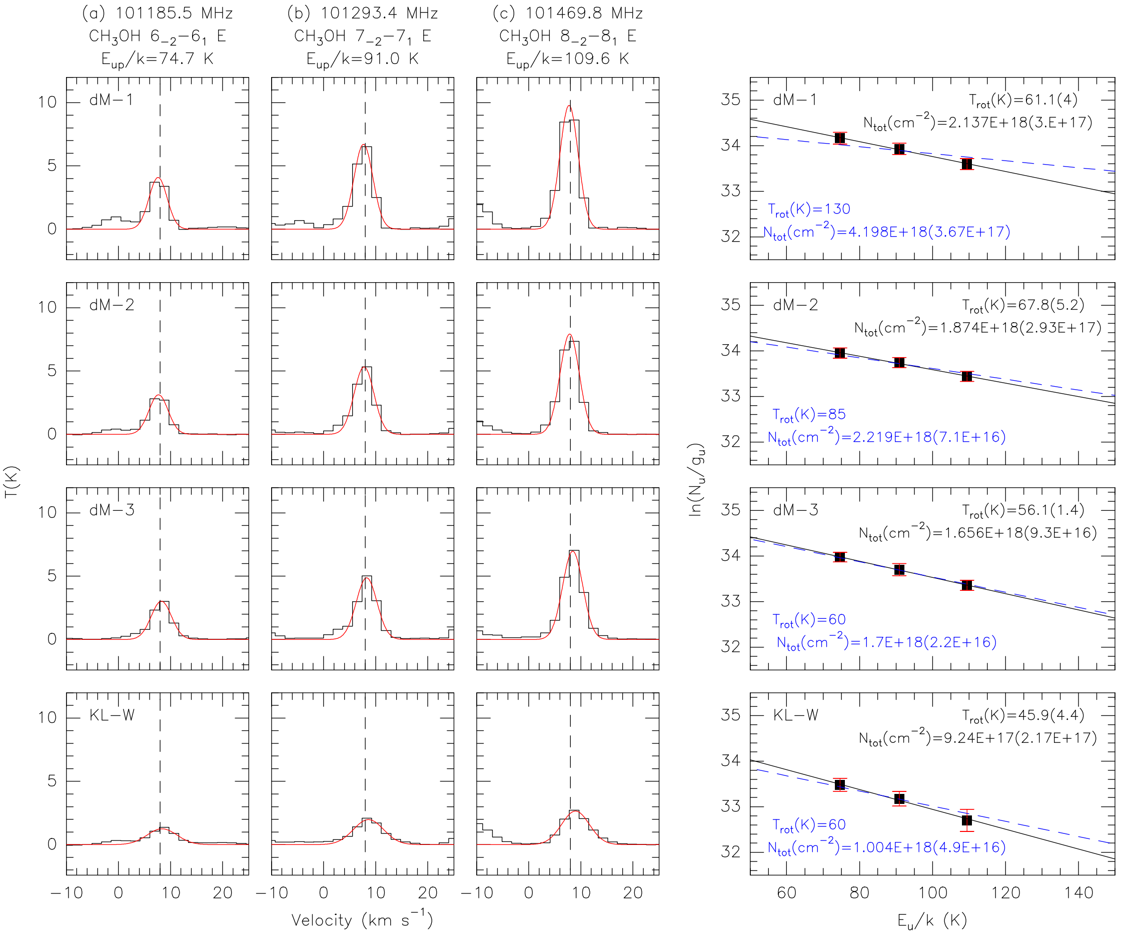

Fig. B.4. CH_3OH spectra ($3\farcs8 \times 2\farcs0$) toward the four positions identified in Fig. 1 in the Orion BN/KL region. The methanol rotational temperatures and column densities are estimated by a least-squares fit, where the uncertainties include the statistical error, the rms noise, and calibration uncertainties (10%). Blue dashed lines indicate the fits with fixed temperatures. Black dashed lines indicate a V_{LSR} of 8 km s^{-1}.

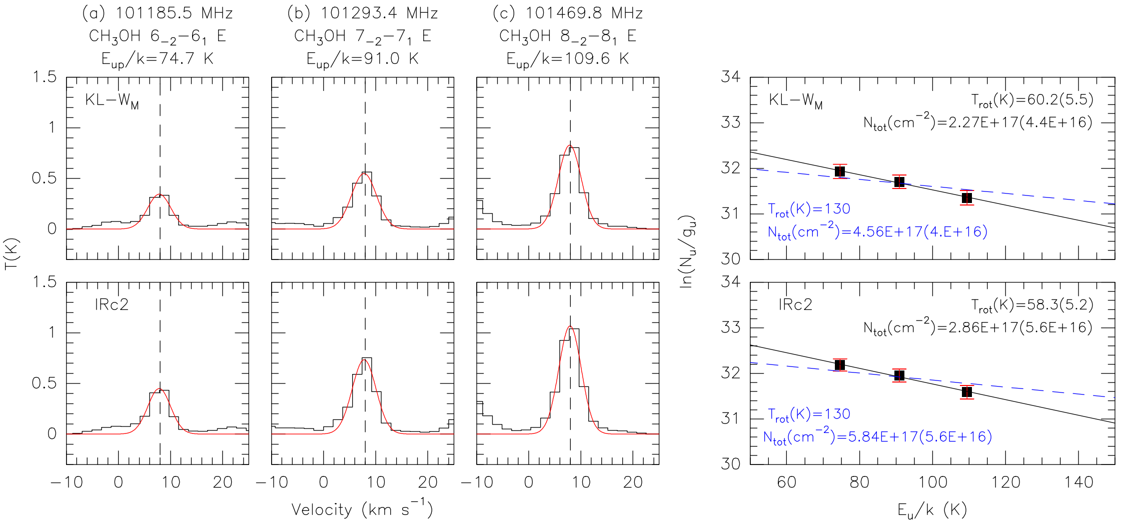

Fig. B.5. Similar plot as Fig. B.4. CH_3OH spectra were smoothed to the 30m beam size of 25″ to compare with the previous 30m observations by Menten et al. (1988). Upper panels show the CH_3OH spectra and population diagram taken at the same position ($05^h35^m14\fs18$, $-05°22'26\farcs5$, J2000) used by Menten et al. (1988) and Mauersberger et al. (1988), which is located about 5″ to the north of KL-W (denoted as KL-W_M). Lower panels show the CH_3OH spectra and population diagram taken at IRc2 ($05^h35^m14\fs47$, $-05°22'30\farcs2$, J2000) used by Jacq et al. (1993). Blue dashed lines indicate the fits with a fixed temperature of 130 K. Black dashed lines indicate a V_{LSR} of 8 km s^{-1}. Note that the CH_3OH column density derived toward KL-W_M is about 20% lower than that of IRc2.

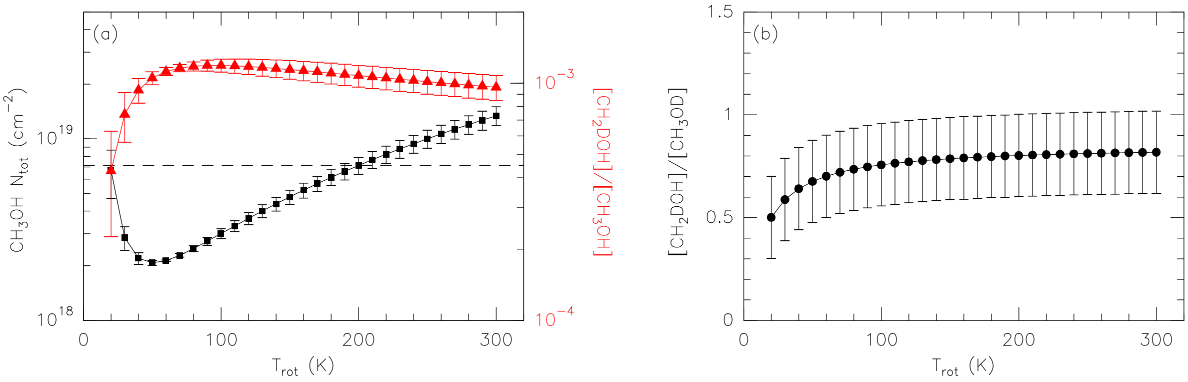

Fig. B.6. (a) Variation of derived CH_3OH column densities with respect to different rotational temperatures toward dM-1. The corresponding $[CH_2DOH]/[CH_3OH]$ abundance (derived in population diagrams) ratios are shown in red. The best-fit result corresponds to a CH_3OH column density of 2.1×10^{18} cm^{-2} and a temperature of about 60 K. For temperatures lower than 200 K, the differences in the derived column densities are clearly smaller than a factor of about 3. The $[CH_2DOH]/[CH_3OH]$ abundance ratios derived from different temperatures are lower than 1.1×10^{-3}. (b) Variation of the relative abundance (based on the ratio of two transitions of CH_2DOH and CH_3OD as seen in Fig. 3 e) of the two isotopologs toward dM-1 as a function of the adopted temperatures. Note that this ratio does not depend much on the temperature.

Table B.2. PdBI CH_3OH line parameters at dM-1, dM-2, dM-3, and KL-W

Frequency (MHz)	Transition (J_k)	E_{up}/k (K)	$S\mu^2$ (D^2)	T_{peak} (K)	V_{LSR} (km s^{-1})	ΔV (km s^{-1})	$\int T dV$ (K km s^{-1})
dM-1 ($05^{\mathrm{h}}35^{\mathrm{m}}14^{\mathrm{s}}.442$, $-05°22'34''.86$)							
101185.4530	$6_{-2} - 6_1$ E	74.7	0.021	3.72 ± 0.05	7.01 ± 0.93	4.09 ± 1.58	17.92 ± 5.56
101293.4150	$7_{-2} - 7_1$ E	91.0	0.046	6.50 ± 0.05	8.31 ± 0.93	4.29 ± 0.95	30.72 ± 5.61
101469.8050	$8_{-2} - 8_1$ E	109.6	0.091	8.59 ± 0.05	7.84 ± 0.93	4.18 ± 0.65	43.49 ± 5.45
dM-2 ($05^{\mathrm{h}}35^{\mathrm{m}}14^{\mathrm{s}}.320$, $-05°22'37''.23$)							
101185.4530	$6_{-2} - 6_1$ E	74.7	0.021	2.70 ± 0.05	7.86 ± 0.93	4.33 ± 1.98	14.48 ± 5.38
101293.4150	$7_{-2} - 7_1$ E	91.0	0.046	5.29 ± 0.05	8.26 ± 0.93	4.48 ± 1.19	25.49 ± 5.52
101469.8050	$8_{-2} - 8_1$ E	109.6	0.091	7.36 ± 0.05	8.76 ± 0.93	4.40 ± 0.75	37.07 ± 5.34
dM-3 ($05^{\mathrm{h}}35^{\mathrm{m}}14^{\mathrm{s}}.107$, $-05°22'37''.43$)							
101185.4530	$6_{-2} - 6_1$ E	74.7	0.021	2.98 ± 0.05	8.81 ± 0.93	4.46 ± 1.82	14.28 ± 4.65
101293.4150	$7_{-2} - 7_1$ E	91.0	0.046	5.00 ± 0.05	8.31 ± 0.93	4.59 ± 1.14	23.78 ± 4.76
101469.8050	$8_{-2} - 8_1$ E	109.6	0.091	6.84 ± 0.05	8.76 ± 0.93	4.54 ± 0.74	33.54 ± 4.62
KL-W ($05^{\mathrm{h}}35^{\mathrm{m}}14^{\mathrm{s}}.159$, $-05°22'28''.25$)							
101185.4530	$6_{-2} - 6_1$ E	74.7	0.021	2.70 ± 0.05	8.76 ± 0.93	6.52 ± 6.13	8.65 ± 6.05
101293.4150	$7_{-2} - 7_1$ E	91.0	0.046	4.16 ± 0.05	8.31 ± 0.93	6.72 ± 3.44	14.09 ± 5.65
101469.8050	$8_{-2} - 8_1$ E	109.6	0.091	5.40 ± 0.05	8.76 ± 0.93	6.17 ± 2.24	17.38 ± 5.25

Notes. The R.A. and Dec. coordinates at the J2000.0 epoch are given for the four sources. Frequency, E_{up}/k, and $S\mu^2$ data were taken from the JPL database. The V_{LSR} is measured at the peak temperatures, and the line widths and integrated intensities are estimated by fitting a Gaussian profile.

Table B.3. PdBI CH_3OD $5_{-1} - 4_{-1}$ E line parameters at dM-1, dM-2, and dM-3

Position	T_{peak} (K)	V_{LSR} (km s^{-1})	ΔV (km s^{-1})	$\int T dV$ (K km s^{-1})	Comment
dM-1	1.91 ± 0.24	7.69 ± 0.42	2.19 ± 0.42	4.47 ± 0.27	
dM-2	1.82 ± 0.22	7.58 ± 0.42	2.87 ± 0.42	5.55 ± 0.36	
dM-3	1.60 ± 0.30	7.43 ± 0.42	1.39 ± 0.42	2.36 ± 0.21	1st component
	0.83 ± 0.27	9.28 ± 0.42	1.94 ± 0.41	1.71 ± 0.28	2nd component